Rationally constructing metastable ZrO_2 supported Ni catalysts for highly efficient and stable dry reforming of methane

Meng Zhang [a,*], Tao Yang [a], Kai Jiang [a], Yongzhen Gao [a], Jingyi Yang [b], Zhongyi Liu [a,c,**], Yizhuo Han [d,*]

[a] College of Chemistry, Zhengzhou University, Zhengzhou 450001, PR China
[b] School of Chemical Engineering, Zhengzhou University, Zhengzhou 450001, PR China
[c] State Key Laboratory of Coking Coal Resources Green Exploitation, Zhengzhou University, Zhengzhou 450001, PR China
[d] State Key Laboratory of Coal Conversion, Institute of Coal Chemistry, Chinese Academy of Sciences, Taiyuan 030001, PR China

ARTICLE INFO

ABSTRACT

The metastable Ni/ZrO_2 catalysts were rationally constructed via reflux treatment and employed for dry reforming of methane. Reflux could suppress the transformation and improve the stability of the metastable ZrO_2, as well as enrich its pore structure. Meanwhile, acidity-basicity, Zr^{3+} and oxygen vacancies were also promoted. Additionally, Ni dispersion was remarkably improved with increasing reflux time due to the abundant pores and enhanced metal-support interaction. These results illustrated the evaluation that prolonging reflux time could significantly proliferate the performance of Ni/ZrO_2. Besides, reflux could strengthen the anti-carbon ability but the widened gap between CH_4 dissociation and CO_2 activation would cause more carbon deposition. The catalyst with reflux for 240 h showed the robust stability for 9000 min (CH_4 conversion: 80 %; CO_2 conversion: 88 %) at 750 °C. Furthermore, the mechanisms were discussed to unravel the origin of the accelerated performance by reflux and provide some references for designing efficient Ni-based catalyst.
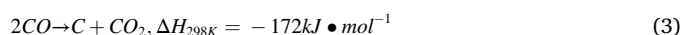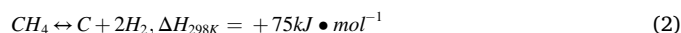
1. Introduction

As is known to all, CH_4 and CO_2 are two main greenhouse gases [1–3], which are responsible for the fraught global warming. Therefore, the great efforts have been made to capture, use and storage these greenhouse gases in academia and industrial. Among the investigated approaches, dry reforming of methane (DRM, Eq. 1) is a promising route to simultaneously convert CH_4 and CO_2 into the highly valuable syngas (H_2 and CO) with nearly uniform H_2/CO ratio, which is suitable for oxo-synthesis and Fischer-Tropsch synthesis [3–5]. Hence, it is of vital importance to develop the efficient and robust catalyst for DRM.

$$CH_4 + CO_2 \leftrightarrow 2H_2 + 2CO, \Delta H_{298K} = +247kJ \bullet mol^{-1} \quad (1)$$
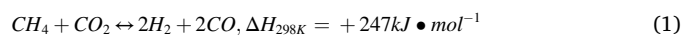
Due to the strongly endothermic nature of DRM and the chemical inertness of CH_4 and CO_2 molecules, DRM is often proceeded at the temperature above 700 °C to obtain the remarkable conversion of the reactants [6,7]. Although the noble metal catalysts exhibit the excellent activity, the expensive price makes the large-scale application

prohibitive [8]. The extensive consistency demonstrates Ni-based catalysts with the cheap price and comparable activity are the ideal choice. However, the operation temperature is higher than its Tammann temperature (590 °C) [9]. Therefore, it is still a crucial issue to avoid the sintering of the active metal Ni.

Additionally, the deposited carbon caused by CH_4 cracking (Eq. 2) and CO disproportionation (Eq. 3) would also deactivate the Ni-based catalysts [4,10]. On one hand, smaller Ni particles exhibit better performance and stronger resistance for carbon deposition [2,7,11]. On the other hand, the support with rich oxygen vacancies and basicity sites can enhance CO_2 activation, which would narrow the gap between carbon accumulation and elimination, thereby reducing carbon deposition [12–14]. It is reasonable that developing the efficient and stable Ni-based DRM catalysts should focus on the novel strategies to improve Ni dispersion and avoid sintering, as well as carbon deposition.

$$CH_4 \leftrightarrow C + 2H_2, \Delta H_{298K} = +75kJ \bullet mol^{-1} \quad (2)$$

$$2CO \rightarrow C + CO_2, \Delta H_{298K} = -172kJ \bullet mol^{-1} \quad (3)$$

In the past decades, ZrO_2 has been widely applied as an excellent support for DRM due to its high thermal stability, acidity-basicity, and redox properties [15]. Nowadays, Ni-ZrO_2-based catalysts are still considered to be an alternative for the industrial application [16,17]. Nevertheless, the complex phase structure transformation at the high operation temperature, accompanied with the channel collapse and surface properties deterioration, makes it difficult to achieve the robust activity [18,19].

Apparently, the insight into the influences of ZrO_2 on the performance is crucial for the design of the efficient catalyst. However, it is arguable to establish the certain correlation between surface properties and ZrO_2 phase structure [20–22], which somewhat limits the comprehension on the catalyst design. Interestingly, the significant promotion in the DRM performance by the metastable phase (amorphous (am), and tetragonal (t)) ZrO_2 has been well demonstrated in many open reports [19,23,24] due to their high specific surface area (SSA) and abundant pore structure.

Table S1 gives a brief illustration for the correlation between the preparation parameters and the physical properties of ZrO_2-containing samples, including phase structure, particle size and textural parameters. Notably, the preparation method, calcination atmosphere/temperature and dopant play the vital roles in the formation of the metastable structure. Nevertheless, it is readily observed that the desired metastable structure would be destroyed by high temperature, that is, am- or t-ZrO_2 is prone to transforming into the monoclinic (m-) ZrO_2 at high temperature, specifically in DRM at the inevitable high-temperature operation. It would cause severe sintering of the active Ni particles, accompanied with carbon deposition and catalyst deactivation, since the stable m-ZrO_2 frequently has the low SSA and poor pore channel.

Hydrothermal or solvothermal method [25,26], temperature-programmed evaporation-induced self-assembly [27,28], and metal-organic frameworks as the precursors [29,30] have been developed to prepare the metastable ZrO_2, but the metastable structure is only maintained at the relatively low temperature (generally lower than 500 °C). Fortunately, the reflux treatment on $Zr(OH)_4·xH_2O$ obtained by the precipitation or hydrolysis is effective to keep the metastable structure even at the temperature above 800 °C [19,31–34].

In Table S2, we present the comparative data on the structure, preparation method and performance of the Ni-ZrO_2 based catalysts. As expected, the catalyst after reflux generally exhibits the high activity and excellent stability. But the reflux solution with high pH can dissolve the glass equipment, resulting in the Si residue in the obtained catalyst [19,31]. Moreover, the precipitant cations (mainly K^+ and Na^+) are difficult to be washed thoroughly after reflux [35,36], which might enhance the catalyst basicity, and improve the carbon-resistance ability. Additionally, the Si residue is helpful for stabilizing the metastable structure and improving Ni dispersion. Therefore, many current studies on the effects of reflux on DRM are interfered by too many factors, and the results fail to reveal the essential correlation between ZrO_2 structure optimization after reflux and DRM performance. Much worse, the excessive Si would enhance the undesired acidity and block the pore structure, which even reduce the activity and stability [19,37].

Herein, the reflux treatment on the precipitated $Zr(OH)_4·xH_2O$ was also employed to rationally construct the metastable Ni/ZrO_2 catalyst with high thermal stability. Due to the precipitation slurry with high pH, the followed reflux would cause the undesired residue of Si or alkali ion. Thus, the precipitation slurry was washed thoroughly before the reflux treatment. After washed, the reflux under the neutral conditions was effective to avoid the obstacle of the residues, thereby preventing the effects of residues on understanding the correlation between ZrO_2 structure and DRM performance. Moreover, in combination with a series of characterization data and evaluation experiments, the structure-activity relationship of Ni/ZrO_2 catalyst in DRM was discussed in depth, and the reaction mechanisms were analyzed by the comprehensive *in situ* infrared spectroscopy experiments.

2. Experimental

2.1. Catalyst preparation

The investigated catalysts were prepared using the co-precipitated and reflux method with $Ni(NO_3)_2·6 H_2O$ (purity 98.0 %, Sinopharm Chemical Reagent Co., Ltd) and $ZrOCl_2·8 H_2O$ (purity 99.0 %, Sinopharm Chemical Reagent Co., Ltd) as the precursors. First, Ni $(NO_3)_2·6 H_2O$ and $ZrOCl_2·8 H_2O$ were dissolved into an appropriate amount of deionized water (nominal Ni loading=10 wt %, $c(Zr^{4+})$= 0.5 M). Then, the above solution and KOH aqueous solution (10 wt %) were simultaneously dropped into a beaker under the vigorous stirring at 60 °C (pH=12–13), and the obtained slurry was further stirred for 240 min. Next, the filter cake was washed thoroughly until the filtrate was neutral to remove K^+ ions and avoid the dissolution of Si^{4+} ions during the following reflux process. Subsequently, the cake was re-broken in the deionized water and refluxed at 100 °C for a period of time. Finally, the turbid liquid was filtered, and the resultant filter cake was dried at 110 °C overnight and calcined at 700 °C for 240 min to obtain the calcined catalyst, which was simplified as NZ-Rx, where x was the reflux hours.

2.2. Catalyst characterization

The catalysts were characterized by the techniques of powder X-ray diffraction (PXRD), N_2-sorption, Inductively coupled plasma optical emission spectrometry (ICP-OES), Transmission electron microscopy (TEM), energy-dispersive X-ray spectroscopy (EDS), X-ray photoelectron spectroscopy (XPS), Diffuse reflectance infrared Fourier transform (DRIFT) spectroscopy, H_2 temperature-programmed reduction (H_2-TPR), H_2 chemisorption, H_2 temperature-programmed desorption (H_2-TPD), CO_2-TPD, NH_3-TPD, Thermogravimetry and Raman spectroscopy. The detailed information was described in Supporting information.

2.3. Catalytic activity evaluation

The DRM activity evaluation was performed on a micro quartz tube reactor with an internal diameter of 6 mm under the atmospheric pressure. For each test, the catalyst (200 mg, 20–40 meshes), diluted with the quartz sand (1000 mg, 20–40 meshes), was placed at the center of the reactor. The sample was firstly reduced at 700 °C for 60 min in the flow of 10 vol % H_2/Ar (30 mL·min^{-1}). Then, the reactant gases (CH_4/CO_2=1/1, weight hourly space velocity (WHSV) = 24000 mL·g^{-1}·min^{-1}) were switched and the effluent gases treated by a cold trap were analyzed by an on-line gas chromatograph equipped with TDX-01 column and thermal conductivity detector. Here, the sample treated at 700 °C for 60 min in the flow of 10 vol % H_2/Ar was named as the reduced one and the sample after evaluated was called as the spent one. The relevant calculation equations about the evaluation were given in Supporting information.

3. Results and discussion

3.1. Structural and morphological properties

Fig. 1a shows the PXRD patterns of the calcined NZ catalysts with different reflux time. It is readily noted that NZ-R0 without reflux exhibits the diffraction peaks indexed to both m-ZrO_2 (JCPDS 37–1484) and t-ZrO_2 (JCPDS 79–1769). With the reflux time extended to 24 h, the intensity of the diffraction peaks ascribed to m-ZrO_2 gradually weakens while that assigned to t-ZrO_2 is enhanced. It indicates that the reflux treatment can improve the tetragonal fraction (v_t) in the support, as calculated in Table 1. Moreover, if the reflux time is further prolonged to more than 72 h, only t-ZrO_2 is observed on the patterns. Additionally, the half-width corresponded to the diffraction peaks for both m- and t-ZrO_2, as well as Ni, is broadened with the extended reflux time,
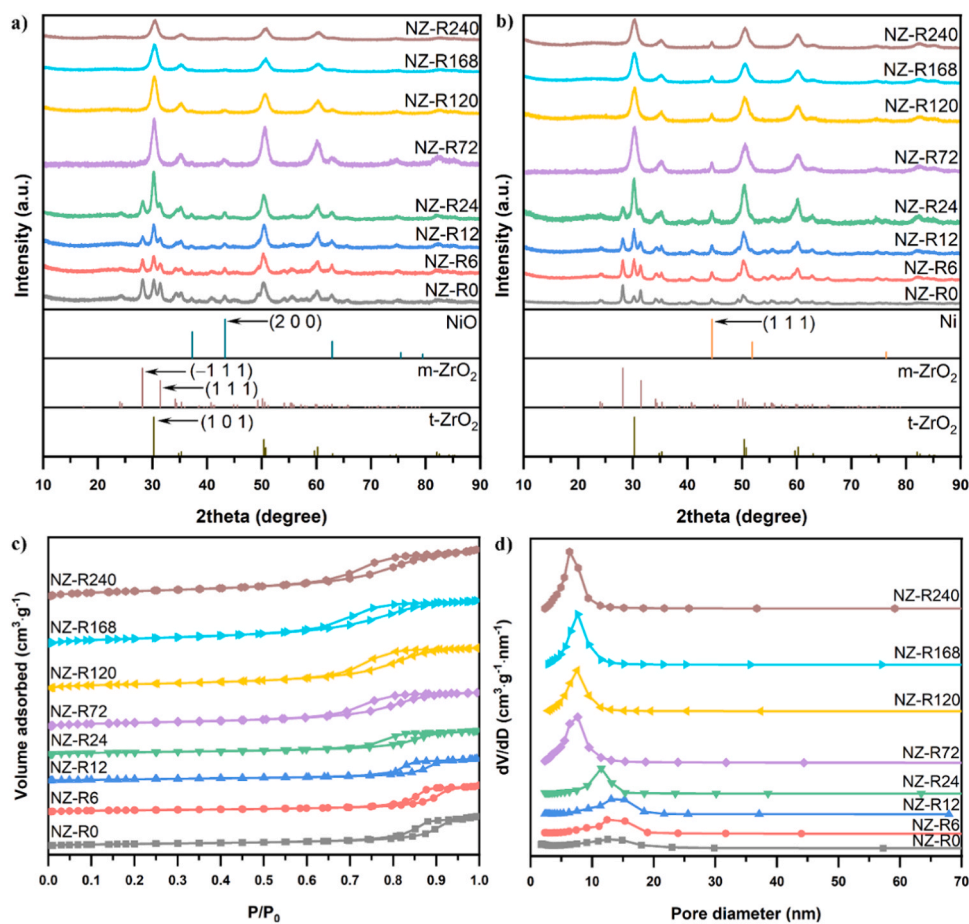
Fig. 1. PXRD patterns of the calcined (a) and reduced (b) NZ catalysts with different reflux time; N_2-sorption isotherms (c) and pore size distributions (d) of the calcined NZ catalysts with different reflux time.

Table 1
Crystalline sizes of ZrO_2, NiO, and Ni, as well as v_t over the calcined and reduced NZ catalysts with different reflux time.

Catalyst	ZrO_2 crystalline size[a] (nm)		v_t[b] (%)	NiO crystalline size[c] (nm)	Ni crystalline size (nm)	
	m	t			d_1[d]	d_2[e]
NZ-R0	20/22[f]	25/28	27/16	17.3	17.7	18.4
NZ-R6	17/19	21/25	39/32	15.7	16.3	17.3
NZ-R12	15/17	18/21	55/39	14.3	16.6	16.4
NZ-R24	13/15	17/19	64/59	13.6	15.7	15.6
NZ-R72	-	15/18	100/100	12.4	15.2	14.5
NZ-R120	-	14/16	100/100	11.8	13.9	13.3
NZ-R168	-	12/14	100/100	11.0	12.7	12.5
NZ-R240	-	11/13	100/100	10.2	11.8	11.8

[a] Calculated using Eq. S1 based on (−1 1 1) and (1 0 1) peaks in Figs. 1a and 1b, respectively.
[b] Calculated using Eq. S2-S4.
[c] Calculated using Eq. S1 based on (2 0 0) peak in Fig. 1a.
[d] Calculated using Eq. S1 based on (1 1 1) peak in Fig. 1b.
[e] Obtained from the TEM data in Fig. S1.
[f] Data before and after the slashes calculated according to the patterns in Figs. 1a and 1b, respectively.

suggesting the decreased crystalline size (detailed data are listed in Table 1). The similar phenomena are observed on the reduced NZ catalysts (Fig. 1b), further verifying the stabilized effects of reflux on the metastable t-ZrO_2. Besides, it should be pointed out that the reflux treatment can reduce Ni particle size, that is, promote Ni dispersion. However, from Table 1, the ZrO_2 crystalline size on the reduced samples is slightly larger than that corresponding to the calcined samples, implying that the reduction process would cause particle agglomeration.

Fig. 1c displays the N_2-sorption isotherms of the as-prepared NZ catalysts. The typical type IV isotherms and H3 hysteresis loops present on all samples, indicating the characteristic mesoporous structure. Notably, with prolonging the reflux time, the loop area gradually enlarges and the initial P/P_0 value tends to decrease, illustrating that reflux enriches the mesoporous structure. The pore size distributions in Fig. 1d, and specific surface area (SSA), pore volume (V_p) and average pore size in Table 2 also confirm the above analysis. According to the XRD patterns (Figs. 1a and 1b), the extension of reflux time suppresses the phase transformation of ZrO_2 and stabilizes the support as the metastable t-ZrO_2. Comprehensively, reflux can improve the stability of the metastable ZrO_2, which is conducive to obtaining the abundant pores, and thus improving Ni dispersion.

The actual Ni loadings on the representative NZ catalysts were determined by the ICP-OES (Table 2), which are close to the nominal value (10 %). Fig. 2a-h depict the TEM images of the reduced NZ catalysts. Apparently, the particle size shows a decreased trend with the increased reflux time, which is consistent with the PXRD results. Further, the distributions of Ni particle size were counted and the data are given in Fig. S1 and Table 2. It can be noted that the reflux treatment not only reduces the average size of Ni particles but also narrows the

Table 2

Characterization and evaluation of the employed NZ catalysts with different reflux time.

Catalyst	NZ-R0	NZ-R6	NZ-R12	NZ-R24	NZ-R72	NZ-R120	NZ-R168	NZ-R240
Ni loading[a]	9.77	9.68	9.67	9.65	9.71	9.58	9.47	9.55
SSA ($m^2 \cdot g^{-1}$)[b]	34	38	44	51	83	97	119	148
V_p ($cm^3 \cdot g^{-1}$)[c]	0.13	0.17	0.16	0.15	0.22	0.26	0.29	0.32
Average pore size (nm)[c]	11	13	13	9	8	8	7	7
Ni dispersion (%)[d]	4.7	5.1	5.7	6.1	6.8	7.5	8.2	8.8
NH_3 desorption amount ($\mu mol \cdot g^{-1}$)[e]	19	25	24	32	48	61	84	102
CO_2 desorption amount ($\mu mol \cdot g^{-1}$)[f]	24	28	26	31	45	52	67	88
Surface Ni mass concentration (%)[g]	5.87	5.49	5.56	5.02	4.74	4.16	3.58	3.22
CH_4 conversion (%)[h]	8.8	10.2	11.7	14.1	16.5	18.8	20.4	24.2
Turnover frequency (s^{-1})[i]	0.17	0.18	0.19	0.21	0.22	0.23	0.23	0.25

[a] Determined by ICP-OES.

[b] Obtained by N_2-sorption using Brunauer-Emmett-Teller method.

[c] Obtained by N_2-sorption using Barrett-Joyner-Halenda model.

[d] Estimated by H_2 chemisorption at 50 °C.

[e] Quantified from NH_3-TPD profiles (Fig. 3b).

[f] Quantified from CO_2-TPD profiles (Fig. 3c).

[g] Determined by XPS spectra of Ni 2p on the calcined catalysts (Fig. 4a).

[h] Evaluated at 500 °C with WHSV of 24000 $mL \cdot g^{-1} \cdot min^{-1}$.

[i] Calculated as the number of CH_4 converted per second per Ni active site at 500 °C using Eq. S8.
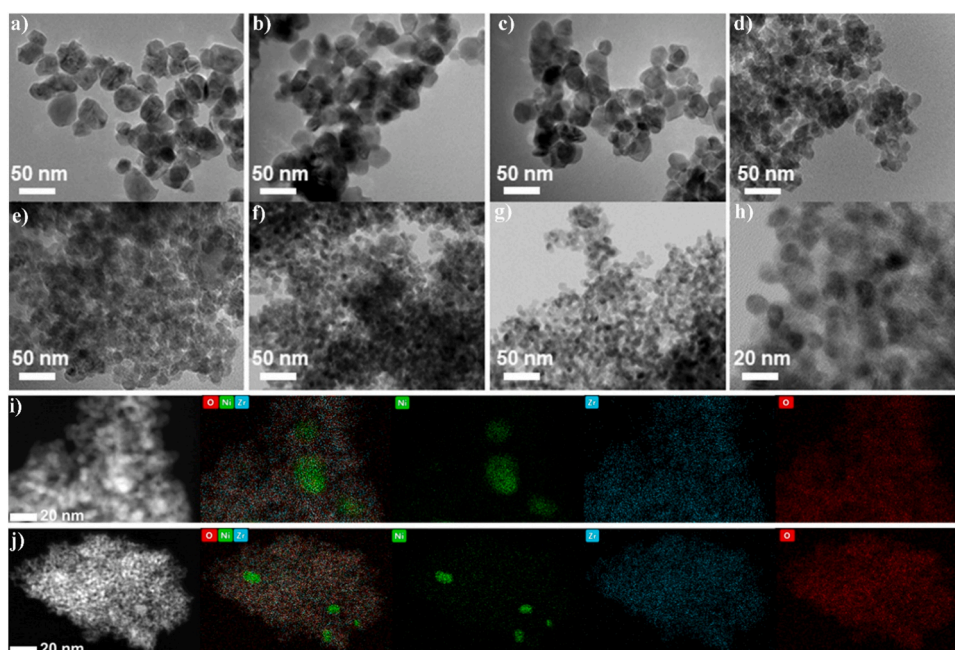
Fig. 2. TEM images of the reduced NZ catalysts with reflux different time (a: NZ-R0, b: NZ-R6, c: NZ-R12, d: NZ-R24, e: NZ-R72, f: NZ-120, g: NZ-R168, and f: NZ-R240); HADDF images and the corresponding elemental mappings of NZ-R0 (i) and NZ-R240 (j).

particle distribution, which has been well demonstrated to be beneficial for DRM [38–40]. Besides, the elemental mappings of NZ-R0 and NZ-R240 are provided in Figs. 2i and 2j. Notably, the size of Ni particles on the latter is lower than that on the former, which further identifies the aforementioned analysis that the reflux treatment promotes Ni dispersion.

3.2. Surface chemical properties

Fig. 3a displays the H_2-TPR profiles of the employed NZ catalysts. The reduction behaviors are closely related to the metal-support interaction (MSI) and Ni particle size [41,42]. The profiles consist of two peaks, where the low-temperature peak is assigned to the reduction of the NiO species isolated on the surface or weakly interacted with ZrO_2 [43,44], while the high-temperature peak is ascribed to the reduction of the NiO species strongly interacted with ZrO_2 [19,45]. Notably, with

increasing the reflux time, the reduction temperature at the initial and summit also increases, indicating the enhanced MSI. Moreover, it can be noted that the aera of H_2 consumption shows a decreased trend when reflux is operated from 0 h to 240 h, implying a decrease in the reduction degree. It is also caused by the strengthened MSI, which is beneficial for promoting metal dispersion and restraining metal sintering [46,47]. Thus, the TPR results provide a clear explanation for the promoted Ni dispersion with extending the reflux time.

Due to the intrinsic acid-base properties of ZrO_2, NH_3- and CO_2-TPD were conducted to examine and the obtained profiles are given in Figs. 3b and 3c, respectively. Obviously, as the reflux time increases, the catalyst exhibits more acid-base sites (also verified by the quantified data listed in Table 2). Currently, there is no consensus on the correlation between the structure of ZrO_2 and its surface acid-base properties [20,48]. Our previous work has unraveled that the catalyst with high v_t possesses more acid-base sites [15]. Additionally, the SSA plays the
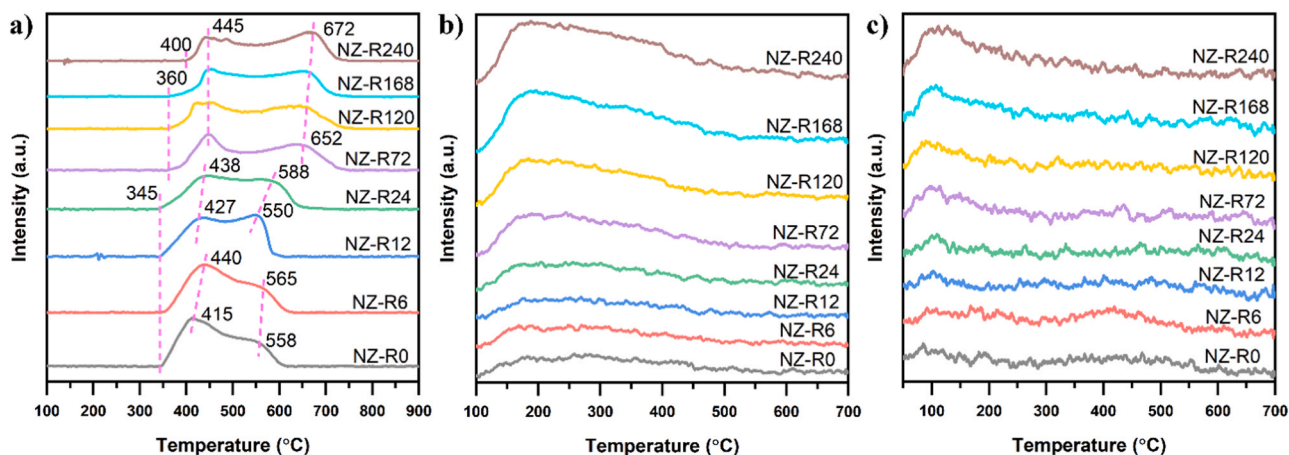
Fig. 3. H_2-TPR (a), NH_3-TPD (b), and CO_2-TPD (c) profiles of the NZ catalysts with different reflux time.

positive role in the amounts of acid-base sites [49]. Here, the above PXRD and N_2-sorption techniques have demonstrated that the reflux treatment would improve v_t value and SSA. Therefore, it is reasonable to reach the aforementioned conclusion that the catalyst with longer reflux has stronger acdity-basicity.

The XPS spectra of the Ni 2p on the calcined NZ catalysts are depicted in Fig. 4a. The fitting results are listed in Table S3. The binding energies at 855.12–856.53 eV (Ni $2p_{3/2}$) and 872.72–874.13 eV (Ni $2p_{1/2}$) are ascribed to the Ni^{2+} species, and the binding energies at 860.93–862.49 eV and 879.22–880.62 eV are the corresponded satellite peaks [44,50,51]. Notably, the binding energy shifts to higher position as the reflux time increases. Besides, the surface Ni concentration obtained by XPS is much lower than the actual Ni loading determined by ICP-OES (Table 2), suggesting that a part of Ni species might embed in ZrO_2 lattice. However, the spectra intensity shows a decreased trend with the extending reflux time, indicating an increase in the amount of Ni species inserted into the support (Table 2). These results illustrate that the interaction between Ni and ZrO_2 is enhanced via reflux, which is in good agreement with the TPR data.

As shown in Fig. S2, the binding energies at approximately 182 and 184 eV are attributed to Zr $3d_{5/2}$ and Zr $3d_{3/2}$, respectively [41]. It is noted that the peak position shifts to lower value with increasing the reflux time, indicating that the reflux time can increase the Zr^{3+} content on the catalyst surface [21,43,52]. The fitted spectra of Zr 3d based on the previous reports [20,21,53] are displayed in Fig. 4b and the quantified data are listed in Table S4. It further verifies the increased Zr^{3+} content on the catalyst with longer reflux time. The open researches

have demonstrated that t-ZrO_2 has more partially reduced Zr species than m-ZrO_2 [15,54]. Our current analysis is consistent with this viewpoint. Moreover, the shift of the binding energies for Ni 2p and Zr 3d is opposite, indicating the interaction and electron transfer between Ni and ZrO_2. Particularly, the shift becomes more significant with longer reflux time, indicating an enhanced MSI.

Fig. 4c displays the spectra of O 1 s on the calcined NZ catalysts with different reflux time, and the fitting results are tabulated in Table S4. The binding energy at about 530 eV (O_α) and 531 eV (O_β) are attributed to surface lattice oxygen (O^{2-}) and adsorbed oxygen (O_2^-/O_2^{2-}) [41,55–57]. The ratio of O_β/O_α (Table S4) represents the concentration of oxygen vacancies [41,58]. The data unravel that the longer the reflux time, the more the oxygen vacancies on the catalyst surface. The analysis of XPS further illustrates that the reflux treatment not only enhances the MSI but also enriches Zr^{3+} and oxygen vacancies on the catalyst surface. This provides a reasonable explanation for the improvement of the acid-base nature of the catalyst with the prolongation of the reflux time.

Fig. 5a-c show the XPS spectra of Ni 2p, Zr 3d and O 1 s on the reduced NZ catalysts, respectively. In consistent with the calcined ones, the binding energies of Ni^{2+} shift to higher position (Table S5) while those of Zr 3d tend to lower value (Fig. S3) as the reflux time increases. However, the spectra of both Ni^{2+} and Ni^0 can be observed in Fig. 5a and Table S5, which might be due to the re-oxidation of the reduced catalyst. The fitting results O 1 s and Zr 3d are given in Table S6. A decrease in the content of oxygen vacancies and Zr^{3+} occurs after reduction, which is attributed to the transformation in ZrO_2 crystalline phase (NZ-R0~24) and the increase in crystallinity of the metastable structure (NZ-
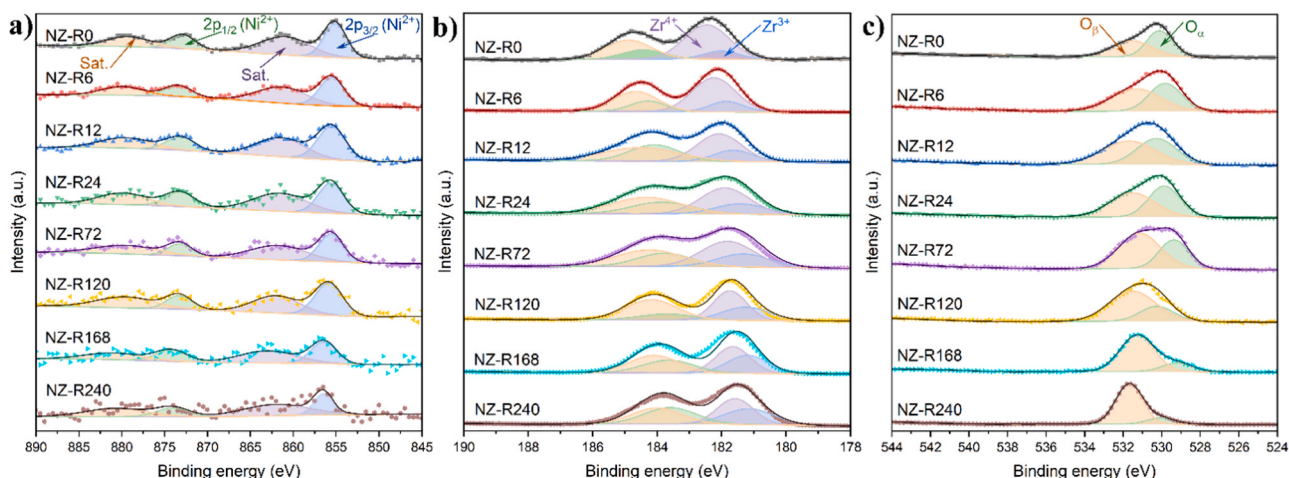

Fig. 4. XPS spectra for Ni 2p (a), Zr 3d (b), and O 1 s (c) on the calcined NZ catalysts with different reflux time.
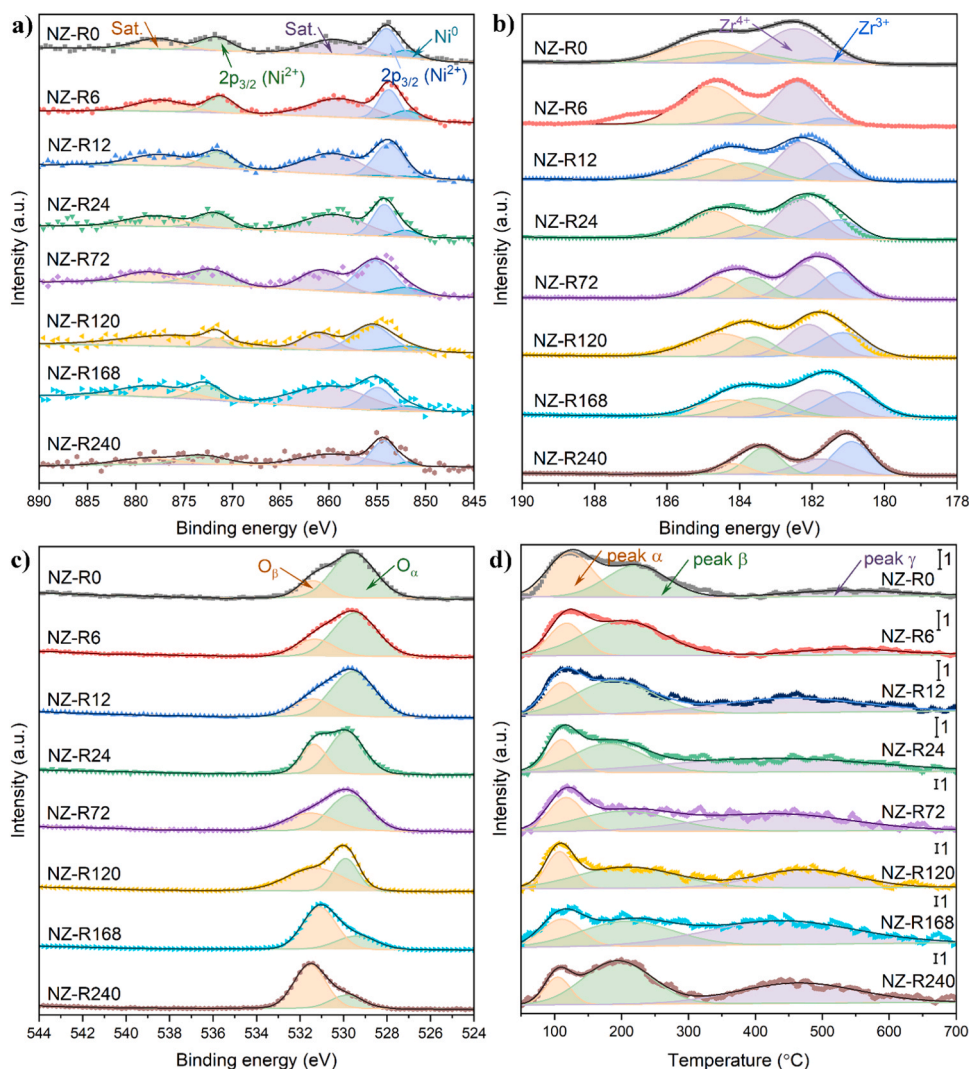
Fig. 5. XPS spectra for Ni 2p (a), Zr 3d (b), and O 1 s (c), and O_2-TPD profiles (d) on the reduced NZ catalysts with different reflux time.

R72~240) during the reduction process. Fig. 5d depicts O_2-TPD profiles of the reduced NZ catalysts. Peaks α, β, and γ are assigned to physically adsorbed oxygen species, loosely and tightly captured oxygen species by the oxygen vacancies, respectively [59]. The data in Table S7 disclosure that the reflux treatment could enhance the capacity for O_2 adsorption. Moreover, the content of oxygen species correlated to oxygen vacancies (peak β and γ) shows a significant increase with the extending reflux time, which is in good agreement with the results of XPS spectra.

The above characterization results clearly indicate that the reflux treatment could increase the ν_t value in the NZ catalyst, and if the time is longer than 72 h, the catalyst with pure metastable ZrO_2 would be obtained. Besides, the SSA is improved and the pore structure is enriched after reflux. Meanwhile, the reflux treatment also significantly enhances the MSI. These factors are essential for promoting Ni dispersion. On the other hand, the studies on the surface properties unravel that the catalyst with high content of the metastable structure has more Zr^{3+}, oxygen vacancies and acid-base sites. Furthermore, for the catalyst containing only t-ZrO_2, the longer the reflux time, the more Zr^{3+} sites and oxygen vacancies on the surface. In the previous literature [19,31,60], despite the reflux time shorter than 240 h, the reflux treatment operated in the alkaline solution would induce the presence of the amorphous structure due to the residual Si or alkaline ions. However, in the present study, reflux is carried out in the neutral solution, and thus, even the time is extended to 240 h, only the tetragonal structure is observed.

3.3. Activity and stability

The activity of the employed NZ catalysts for DRM was carried out at atmospheric pressure and 700 °C with WHSV of 24000 mL·g^{-1}·h^{-1}. As shown in Figs. 6a and 6b, NZ-R0 shows the lowest conversions of CH_4 and CO_2. Moreover, the obvious decline of the activity is readily noted. Apparently, the reflux treatment remarkably promotes the conversions of CH_4 and CO_2. Specifically, the catalyst suffering from longer reflux possesses higher activity. However, when the reflux time is shorter than 24 h, the stability has no noticeable improvement. If the reflux is further extended to beyond 72 h, the catalyst displays the relatively robust stability during the DRM test for 600 min. Overall, the reflux, especially long-term treatment, can effectively improve the DRM performance over the Ni/ZrO_2 catalyst. It further verifies that higher Ni dispersion, stronger acid-base properties, and more oxygen vacancies are beneficial for the conversion of CH_4 and CO_2, as well as deactivation resistance. Due to the inevitable side-reaction (reverse water gas shift reaction, RWGS, Eq. 4), the H_2/CO ratio at the outlet is always lower than 1.0, as depicted in Fig. 6c. Besides, it has been demonstrated that RWGS is more favored over the catalyst with larger Ni nanoparticles [61]. As identified above, the catalyst with longer reflux time has smaller Ni particles. Therefore, it is reasonably noted that the ratio of H_2/CO is higher over the catalyst with longer reflux time.
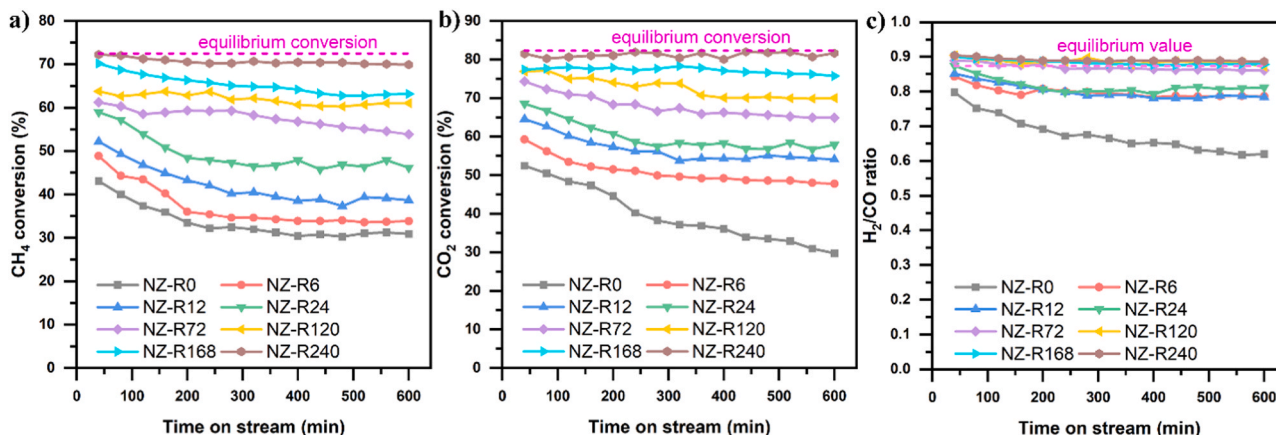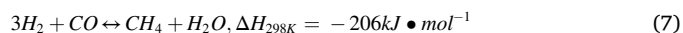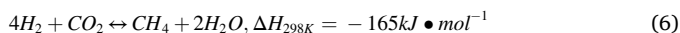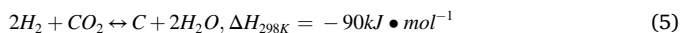
$$H_2 + CO_2 \rightarrow CO + H_2O, \Delta H_{298K} = +41 kJ \bullet mol^{-1} \qquad (4)$$
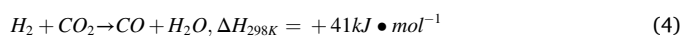
Fig. 6. (a) CH_4 conversion, (b) CO_2 conversion, and (c) H_2/CO ratio during the DRM reaction over the representative NZ catalysts with different reflux time as a function of time on stream.

The effects of the reaction temperature on the reaction activity over NZ-R240 were evaluated at atmospheric pressure with WHSV of 24000 mL·g^{-1}·h^{-1} (CH_4/CO_2=1/1) and the results are given in Fig. 7a. Notably, the increased temperature enhances CH_4 and CO_2 conversion, which is mainly due to the endothermic nature of DRM. Besides, CO_2 conversion is always higher than CH_4 conversion and the ratio of H_2/CO is less than 1.0, indicating the accompanied occurrence of RWGS. The upward H_2/CO ratio with the raised temperature can be ascribed to the fact that the favorable DRM and CH_4 cracking with higher Equilibrium constants would occupy more actives sites, which might weaken RWGS. On the other hand, high temperature somewhat hinders the exothermic side reactions (Eqs. 5-7).

$$2H_2 + CO_2 \leftrightarrow C + 2H_2O, \Delta H_{298K} = -90 kJ \bullet mol^{-1} \qquad (5)$$

$$4H_2 + CO_2 \leftrightarrow CH_4 + 2H_2O, \Delta H_{298K} = -165 kJ \bullet mol^{-1} \qquad (6)$$

$$3H_2 + CO \leftrightarrow CH_4 + H_2O, \Delta H_{298K} = -206 kJ \bullet mol^{-1} \qquad (7)$$

Shown in Fig. 7b is the DRM performance over NZ-R240 at atmospheric pressure and 700 °C with different WHSVs (CH_4/CO_2=1/1). Observably, the increase of the WHSV decreases the conversions of CH_4 and CO_2. Higher WHSV means shorter residence time, and thus, the adsorbed reactants on the catalyst surface suffer from the insufficient contact, leading to the decreased activity. Also, the ratio of H_2/CO tends to decrease with the reduced contact time since RWGS is promoted at higher CO_2 concentration [62].

The stability of NZ-R240 for DRM was performed at atmospheric pressure and 750 °C with WHSV of 24000 mL·g^{-1}·h^{-1}. As displayed in Fig. 7c, NZ-R240 achieves the constant conversions of CH_4 (80 %) and CO_2 (88 %) for 9000 min, which is close to the thermodynamic equilibrium. Additionally, no obvious deactivation is observed. The ratio of H_2/CO in the obtained syngas is near to 1.0 (0.97), which is suitable for
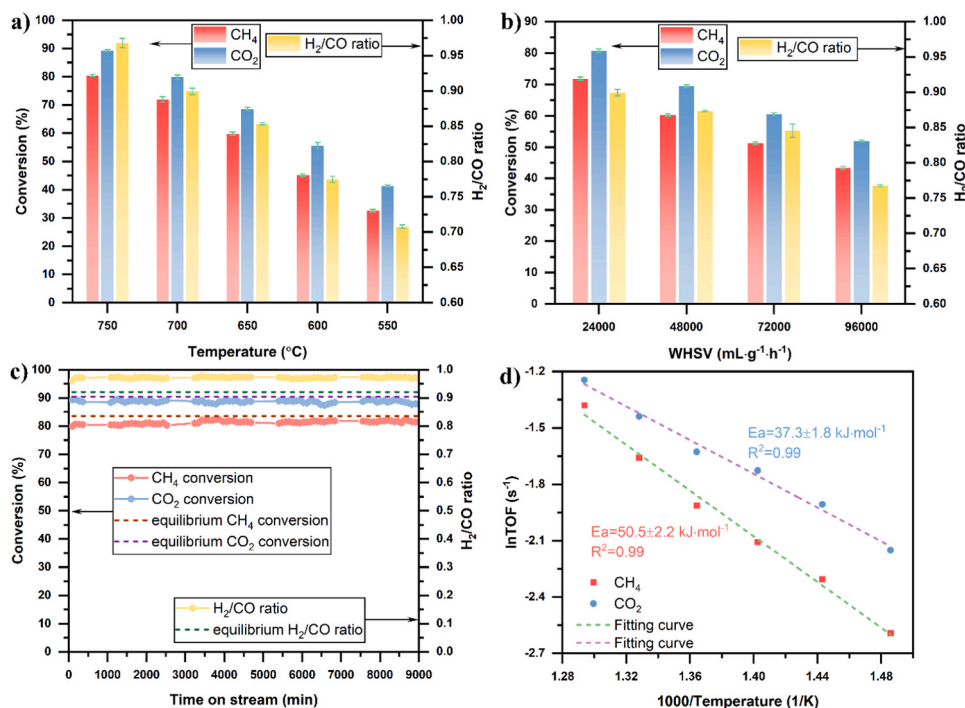

Fig. 7. CH_4 conversion, CO_2 conversion and H_2/CO ratio during DRM over NZ-R240 as a function of temperature (a) and WHSV (b); (c) Long-term stability of NZ-R240 for DRM at 750 °C with WHSV of 24000 mL·g^{-1}·h^{-1}; (d) Arrhenius plots for the value of TOF over NZ-R240 at the temperature range of 400–500 °C with WHSV of 24000 mL·g^{-1}·h^{-1}.

producing hydrocarbons via Fischer-Tropsch synthesis. The ratios higher than the equilibrium might be caused by CH_4 dissociation.

When comparing the DRM performance over NZ-R240 with the available reports on the basis of the Ni-ZrO_2 catalytic system (Table S2), the conversions of CH_4 and CO_2 over NZ-R240 are relatively high. Besides, the stability of NZ-R240 (9000 min) is superior to that over most Ni-ZrO_2-based catalysts, even those modified with promoters. In conjunction with ZrO_2 structure, it can be concluded that the metastable t-ZrO_2 is more favorable for DRM, which is closely related to its high SSA, strong MSI, and abundant surface acid-base sites and oxygen vacancies. The above discussion has proved that the reflux treatment is of vital importance to stabilized the metastable structure. Therefore, the crucial role of reflux in proliferating the DRM performance over the ZrO_2 supported catalysts is worth expecting.

In Table S8, the performance of NZ-R240 is compared with that of Ni catalysts supported by other common supports and noble metal catalysts reported in the literature. It is noticed that NZ-R240 exhibits high activity and robust stability, comparable to that of most Ni catalysts and even surpassing that of noble metal catalysts. Besides, the amount of the deposited carbon is not significant (detailed discussion in Section 3.4). This comparison further illustrates the potential industrial applications of ZrO_2 support.

Furthermore, we have calculated the turnover frequencies (TOF) of the representative NZ catalysts at 500 °C and the data are listed in Table 2. The increase in TOF with the prolonged reflux time suggests that the reflux treatment can enhance the intrinsic activity of the NZ catalysts. This upgrade arises from the improved Ni dispersion and optimized surface properties. The apparent activation energy (Ea) for CH_4 and CO_2 was determined by the Arrhenius formula, and the linear relationship between lnTOF and 1000/T is shown in Fig. 7d. Notably, the activation energy for CO_2 is lower than that for CH_4, which is attributed to the existence of RWGS. Table S9 lists the apparent activation energy over the reported catalysts, and it is evident that the activation energy for CH_4 dissociation is frequently higher than that for CO_2 activation. This implies that CH_4 dissociation remains the determining step for DRM. Therefore, increasing Ni dispersion is still crucial for enhancing CH_4 activation and improving reaction efficiency. Moreover, the present NZ-R240 catalyst employed exhibits the relatively low activation energy, even comparable to the noble metal catalysts, which indicates its potential for widespread application and intensive research.

3.4. Deactivation analysis

Fig. 8a shows the PXRD patterns of the spent NZ catalysts after evaluated for 600 min at 700 °C. On one hand, compared with the patterns of the reduced catalysts (Fig. 1b), the changes in ZrO_2 crystalline phase and Ni crystalline size are noted, especially on the catalysts with reflux time less than 72 h (Table S10). The high reaction
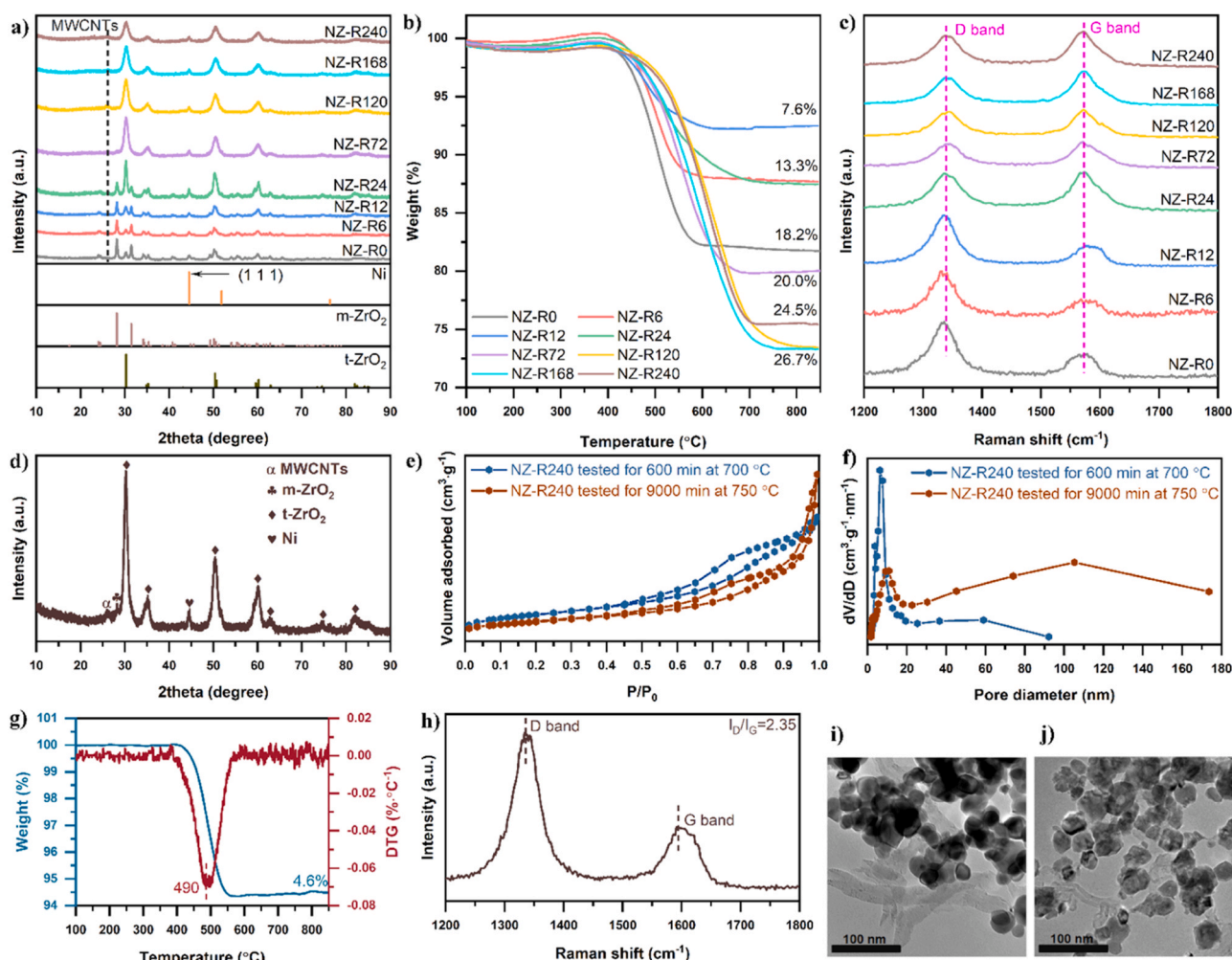
Fig. 8. (a) PXRD patterns, (b) TG profiles, and (c) Raman spectra of the spent NZ catalysts after evaluated at 700 °C for 600 min; (d) PXRD patterns of the spent NZ-R240 catalyst after evaluated at 750 °C for 9000 min; (e) N_2 adsorption-desorption isotherms and (f) pore size distributions of the spent NZ-R240 catalyst; (g) Raman spectra and (h) TG-DTG profiles of the spent NZ-R240 catalyst after evaluated at 750 °C for 9000 min; TEM images of the spent NZ-R240 catalyst (i: at 700 °C for 600 min; j: at 750 °C for 9000 min).

temperature results in the sintering and crystalline transformation of the active metal and the support, which is an important reason for the deactivation. However, it should be emphasized that the catalyst with longer reflux time still has higher v_t. Additionally, for the catalyst with the reflux time more than 72 h, no significant changes in support crystalline phase and Ni crystalline size are observed after evaluation (Table S10). These phenomena suggest that the reflux treatment can improve the thermal stability of the support and the anti-sintering ability of the catalyst. On the other hand, compared with the XRD patterns of the reduced catalysts (Fig. 1b), an obvious diffraction peaks indexed to multi-walled carbon nanotubes (MWCNTs) is present, which suggests that the carbonaceous species are deposited on the catalyst surface. It is also a vital reason to cause the deactivation.

To obtain the amount of carbon deposition, the spent catalysts were characterized by the TG technique (Fig. 8b). It is observed that carbon deposition on NZ-R0 to R12 decreases, while that on NZ-R24 to R168 increases. This indicates that reflux can somewhat enhance the ability of carbon resistance due to the improved Ni dispersion and enriched oxygen vacancies. However, the amount of carbon deposition does not gradually decrease with the increased reflux time. Actually, the catalyst with longer reflux time exhibits a stronger promotion on CH_4 dissociation than that on CO_2 activation, where the former is dominant by Ni dispersion, while the latter is determined by surface properties. The widened gap between CH_4 dissociation and CO_2 activation causes the rate of carbon formation to be faster than that of carbon elimination, resulting in the increased carbon deposition on NZ-R24 to R168. It should be pointed out that NZ-R240 with large amount of carbon deposition does not display an obvious deactivation (Fig. 6). It might be due to that the surface metal sites do not been fully covered by the deposited carbon because the reflux treatment has greatly improved Ni dispersion.

Fig. 8c displays the Raman spectra of the spent catalysts. D (1340 cm^{-1}) and G (1590 cm^{-1}) bands represent the amorphous and graphitic carbon, respectively, and the higher intensity ratio of D and G bands (I_D/I_G) indicates the enhanced reactivity of the deposited carbon [63,64]. The data in Table S10 show that carbon deposition on the catalyst after reflux is more inert, suggesting that the relatively active carbonaceous species can be removed in time. However, due to the unbalanced rate of carbon formation and elimination, the residual carbon becomes more and more inert. DTG profiles in Fig. S4 are the first-order differentiation of TG and its fitting results in Table S11 are also consistent with the conclusion. In summary, although the reflux treatment can improve the anti-carbon ability of the catalyst, the asynchronism between the promoted rate on CH_4 dissociation and CO_2 activation leads to the increased and inert carbon formation on the catalyst after reflux.

Improving the reaction temperature can remarkably enhance the ability to activate CO_2, thereby achieving a balance between carbon deposition and elimination [65,66]. However, the harsh reaction conditions also require higher thermal stability of the catalyst. Fig. 8d displays the PXRD patterns of NZ-R240 after evaluated at 750 °C for 9000 min. Observably, the diffraction peaks indexed to MWCNTs disappear compared to the patterns in Fig. 8a. However, the structure has changed. The diffraction peaks of m-ZrO_2 are visible, and Ni particle size increases (11.8 nm (after reduction) to 14.2 nm (after reaction)). Meanwhile, Figs. 8e and 8f show N_2-sorption isotherms and pore distributions of NZ-R240 after evaluation at different conditions, respectively. It is evident that the mesoporous structure still remains after test at 700 °C, but the test at 750 °C destroys the mesoporous structure. In comparison to fresh sample (SSA: 148 m$^2 \cdot$g^{-1}, V$_p$: 0.32 cm$^3 \cdot$g^{-1}), the decreased in SSA and V$_p$ (127 m$^2 \cdot$g^{-1}, 0.28 cm$^3 \cdot$g^{-1}) on the spent catalyst tested at 700 °C might be attributed to carbon deposition, while that (71 m$^2 \cdot$g^{-1}, 0.20 cm$^3 \cdot$g^{-1}) on the spent catalyst tested at 750 °C is due to the destruction of the high reaction temperature. From Figs. 8g and 8f, it can be noted that the amount of carbon deposition on NZ-R240 test at 750 °C (4.6 %) is much less than that test at 700 °C (24.5 %), and

the reactivity of carbon deposition on the former is higher than that on the latter although the test time at 750 °C is far longer than that at 700 °C. The TEM images in Figs. 8i and 8j also verifies the phenomena. It suggests that improving reaction temperature can effectively accelerate CO_2 activation to somewhat balance carbon formation and elimination. However, carbon deposition still remains inevitable, at least at 750 °C.

3.5. Mechanism study

The aforementioned discussion analyzes the optimization of the structure and properties via reflux, which greatly enhances the performance and resistance to sintering, as well as carbon deposition. In order to better understand the reaction pathways, we systematically investigated the reaction mechanism via the technique of *in situ* DRIFT spectroscopy. Fig. 9 shows the DRIFT spectra of CH_4/CO_2 adsorption on the reduced NZ-R0 and NZ-R240 catalysts at 50 °C. The bands at 3000 and 1304 cm^{-1} in Fig. 9a (the latter also shown in Fig. 9d) are ascribed to the gaseous CH_4, while these at the region of 2400–2200 cm^{-1} are corresponded to the gaseous CO_2 [67]. Fig. 9b displays the spectra at the region of 4000–3200 cm^{-1}, which are corresponded to the surface hydroxyls [68,69]. As shown in Fig. 9c, the bands at the 1650, 1614, and 1540 cm^{-1} are ascribed to COO from bicarbonates (HCO$_3$*), formates (HCO$_2$*), and carbonates (CO$_3$*), respectively [67,70,71]. The bands at 1268 cm^{-1} in Fig. 9d also represent the gaseous CH_4 [70]. The adsorption bands at 1354 and 1341 cm^{-1} displayed in Fig. 9d are assigned to CH_3 species, and the weak bands at 1261 and 1246 cm^{-1} belong to carbonates [72]. The bands at 1221 cm^{-1} in Fig. 9e are related to the vibration of δ(OH) in bicarbonates [71]. Notably, in Figs. 9a and 9d, the intensity of the bands ascribed to the gaseous CH_4 and CO_2 for NZ-R0 is higher than that for NZ-R240, implying the superior adsorption ability for the reactants on the latter.

The detected CH_3 species in Fig. 9d are originated from the direct CH_4 dissociation as follows: $CH_4 \rightarrow CH_3$ (I). Generally, NZ-R240 with higher Ni dispersion should exhibit stronger for CH_4 dissociation [16,73,74], that is, display the stronger band intensity than NZ-R0. Here, the weaker band intensity on NZ-R240 might be ascribed to the deep dissociation of CH_3: $CH_3 \rightarrow CH_2 \rightarrow CH \rightarrow C$ (II).

The bicarbonate and carbonate species are derived from CO_2 adsorption on hydroxyls and vacancies, respectively [75,76]. The remarkable stronger bands of bicarbonates and carbonates on NZ-R240 illustrate the promoted ability for CO_2 activation by the enriched surface oxygen species, as revealed by XPS. Besides, the bicarbonate species are active and can be hydrogenated to be formates: $HCO_3^* + 2H \rightarrow HCO_2^* + H_2O$ (III) [67]. The higher intensity of formats on NZ-R240 provides the explanation for the consumed CH_3 species.

Fig. S5a and S5b depict the survey DRIFT spectra of CH_4/CO_2 temperature-programmed reaction experiment over NZ-R0 and NZ-R240, respectively. As the temperature gradually increases, the intensity of the gaseous CO_2 decreases while that of the gaseous CH_4 has no significant change (also depicted in Fig. 10a2, a5 and b2, b5), illustrating that the increased temperature promotes CO_2 activation but the promotional effect on CH_4 dissociation is unobvious. It is consistent with the aforementioned analysis that the apparent activation energy for CH_4 is higher than that for CO_2. Additionally, the band intensity of the gaseous reactant for NZ-R0 is always higher than that for NZ-R240, implying better reactivity on the latter.

Fig. 10a1 and b1 display the hydroxyl groups. It is observed that the positive bands (shown in Fig. 9b) turn to be negative with the increased temperature, illustrating that the reactants (CH_4) or intermediates (CH$_x$ (x=0–3) or H) would interact with them. As shown in Fig. 10a4 and b4, the band intensity for the bicarbonate species decreases, even to be negative, but that for formates and carbonates (1540 and 1450–1410 cm^{-1}) is enhanced with increasing temperature. It indicates that bicarbonates are the most active species and would react with H into formats, carbonates and CO (Pathway III~VI). The bands at 2077 cm^{-1} in Fig. 10a3 and 10b3 are ascribed to the Ni carbonyl species
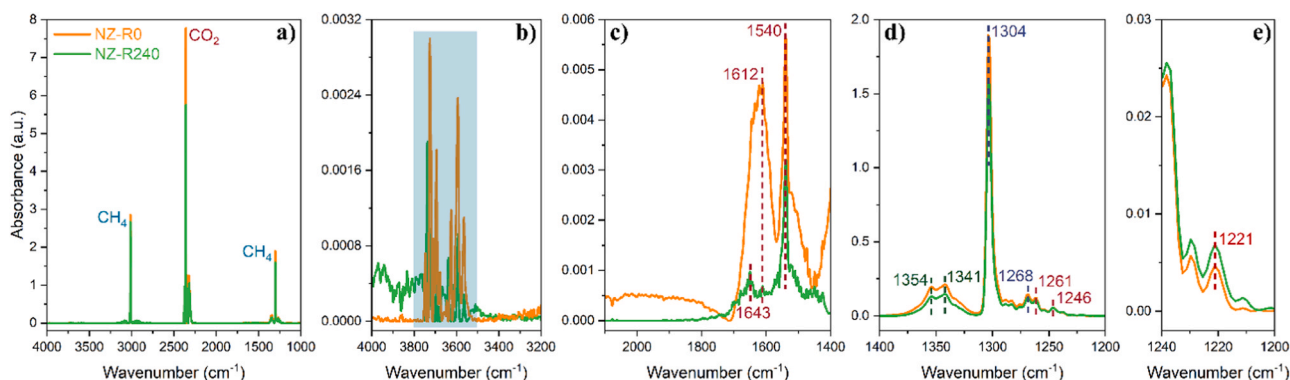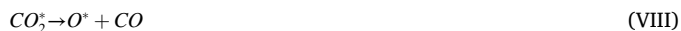
Fig. 9. DRIFT spectra of CH_4/CO_2 adsorption on the reduced NZ-R0 and NZ-R240 catalysts at 50 °C.

on NZ-R0 and NZ-R240, respectively [77]. The higher intensity on the latter suggests more CO is produced, which might obey the following pathways:

$$HCO_2^* + H \rightarrow CO_2^* + H_2 \tag{IV}$$

$$CO_2^* + H \rightarrow OH^* + CO \tag{V}$$

$$HCO_2^* + H \rightarrow H_2O + CO \tag{VI}$$

$$CO_3^* + 2H \rightarrow H_2O + CO \tag{VII}$$

$$CO_2^* \rightarrow O^* + CO \tag{VIII}$$

$$O^* + CH_x \rightarrow CO + xH \quad (x = 0 \sim 4) \tag{IX}$$

Moreover, the increased band intensity of Ni carbonyl on both NZ-R0 and NZ-R240 reveals that higher temperature is beneficial for accelerating the activation of the reactants. Compared the bands in Fig. 10a1-a5 and b1–9b5, it is obvious that the reactivity of the reactants is higher on NZ-R240 that on NZ-R0, further identifying the superior DRM performance over the former.

Furthermore, the DRIFT spectra of the DRM reaction were also collected. From the survey spectra in Fig. S6, it is noted that the bands assigned to the gaseous reactants are still sharper for NZ-R0 than that for NZ-R240, in good agreement with the above discussion. Besides, the band intensity in Fig. S6 (also including the bands in Fig. 10c2, d2 and c5, d5) displays an increased trend with the extended time. It indicates that the activation ability on the representative catalysts somewhat decreases, illustrating that the catalyst suffers from the deactivation. According to the bands in Fig. 10c3 and c4, it can be also concluded that NZ-R240 exhibits higher ability to motivate the reactants, and compared their intensity with these in Fig. 10a3 and a4, apparently, higher temperature is advantage for DRM. The changes of the bands in Fig. 10c1, c4 and d1, d4 further identifies the evolution of the active intermediates.

Fig. 11a-c depicts the DRIFT spectra of CH_4 activation over NZ-R240 with the increased temperature. As shown in Fig. 11a, the hydroxyls at 3850 cm^{-1} (might be involved in H_2O) are detected and the intensity is improved as the temperature increases, which indicates the facilitated CH_4 activation with surface oxygen species. The recorded Ni carbonyl species in Fig. 11b suggest that the carbonaceous species derived from CH_4 could react with the surface oxygen species to produce CO. Besides, the bicarbonates at 1643 cm^{-1} in Fig. 11b first increases then decreases, implying that the oxygen species would interact with the carbonaceous species derived from CH_4 as follows: $3O^* + CH_x \rightarrow HCO_3^* + 2* + (x-1)H(X)$, and high temperature expedites their transformation into carbonates (see the increased intensity at 1540, 1483, and 1450–1410 cm^{-1}). The negative bands for formates illustrate that they participate in the pathways of (IV) and (VI).

When the activation experiment is further operated at 400 °C, the intensity of the hydroxyls at 3850 and 3800–3600 cm^{-1} (Fig. 11d)

gradually increases with the extension of time, illustrating the enhanced CH_4 dissociation, also verified by the comparison on the band intensity in Figs. 11c and 11f. Moreover, the evolution of the carbonates in Fig. 11e further confirms that the surface oxygen species would react with the carbonaceous species originated from CH_4 cracking. After CH_4 activation, CO_2 was switched into the cell and the collected spectra are shown in Fig. 11g. Obviously, more carbonates are formed, suggesting that although the reactive oxygen species are consumed by CH_4, the exposed oxygen vacancies can capture CO_2 to re-generate the active intermediates.

Also, *in situ* DRIFT spectra of CO_2 activation with the increased temperature are recorded and depicted in Fig. 12a. It is noted that CO_2 adsorbed on NZ-R240 could form the bicarbonates (1650 cm^{-1}) and carbonates (bridged: 1585 and 1260 cm^{-1}; bidentate: 1530 cm^{-1}; polydentate: 1485 cm^{-1}; and monodentate: 1445 and 1410 cm^{-1}) [71]. As the temperature raises, the intensity of bicarbonates decreases, and even turn to the inverted peaks, further suggesting their high reactivity with the carbonaceous (CHx) and H species. Meanwhile, the bands ascribed to the carbonates become stronger, illustrating the proliferative CO_2 activation. Besides, the observed Ni carbonyl species (2077 cm^{-1}) imply the formation of CO, which might be derived from CO_2 direct dissociation on the oxygen vacancies or reduced by the metal Ni. When the experiment was further proceeded at 400 °C (Fig. 12b), the bands corresponded to carbonates are enhanced, indicating the continuous CO_2 activation. After CO_2 activation, CH_4 was admitted into the chamber, and the collected spectra are displayed in Fig. 12c. It is apparent that CH_4 can interact with the surface carbonates, which implies that the carbonaceous species could be somewhat removed by the carbonate intermediates, and the released active sites would combine with CO_2 to produce the active intermediates, in good agreement with the above discussion.

In combination with the aforementioned spectra analysis, the well-recognized bi-functional mechanisms are further demonstrated. Specially, CH_4 dissociation occurs on the active metal Ni surface, while CO_2 activation takes place on the ZrO_2 support surface, including the hydroxyl groups, oxygen vacancies, and basic sites. The carbonaceous species originated from CH_4 cracking would react with the active carbonates to form CO and H_2. Thus, the catalyst after reflux with higher Ni dispersion and more reactive oxygen surface exhibits better activity. If the formation rate of the carbonaceous species is higher than the removal rate, coke would deposit on the catalyst surface. However, the rate for CO_2 activation to remove carbon is slower than that for CH_4 dissociation to generate carbon. Therefore, the deposited carbon in DRM is unavoidable. Improving the reaction temperature can somewhat balance the gap between carbon formation and elimination via significantly accelerating CO_2 activation. But the harsh temperature would destroy the catalyst structure, which is also a severe challenge for achieving the robust stability. How to obtain the metastable ZrO_2 with higher thermal stability is still a crucial issue for the stable Ni-ZrO_2
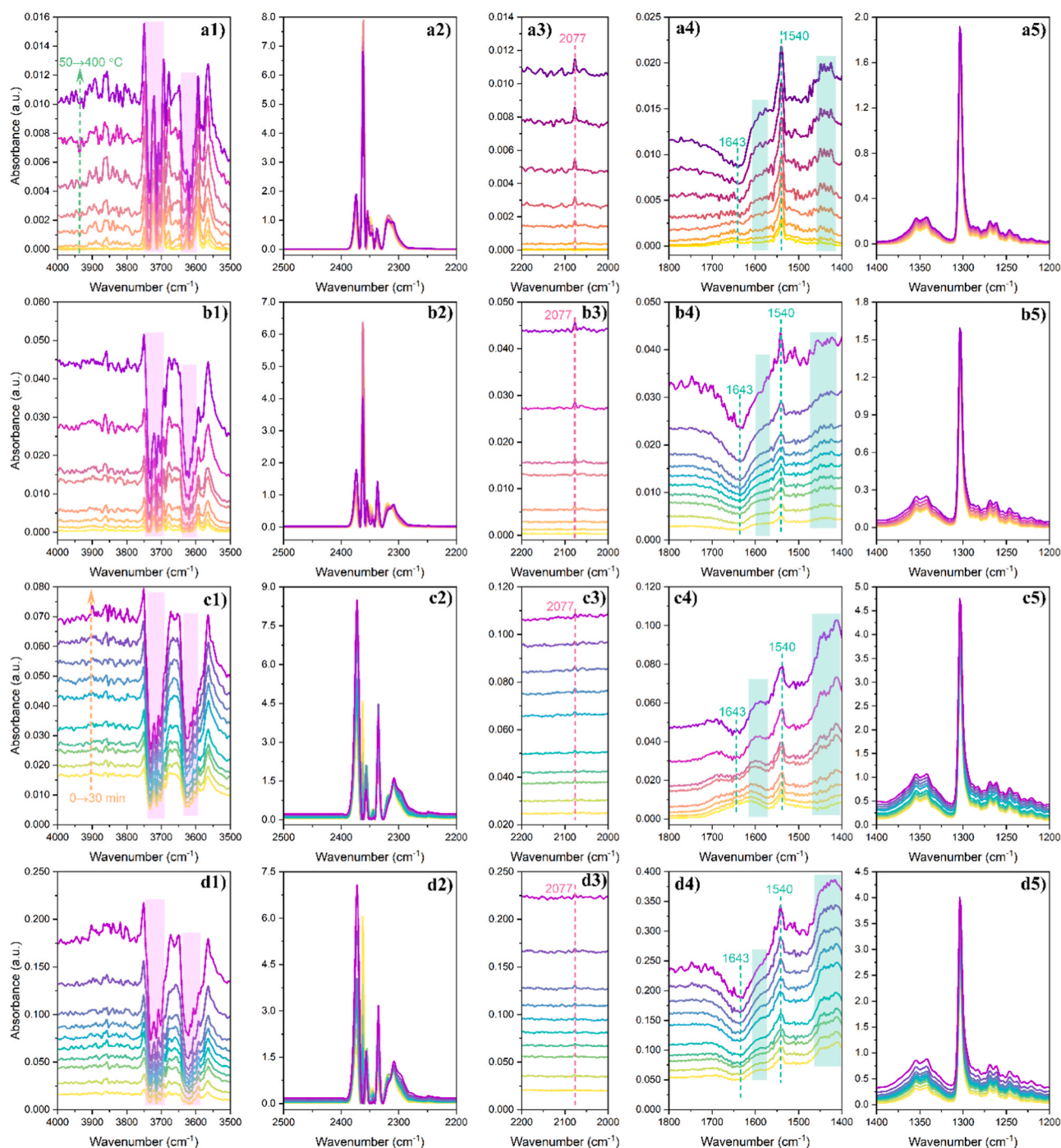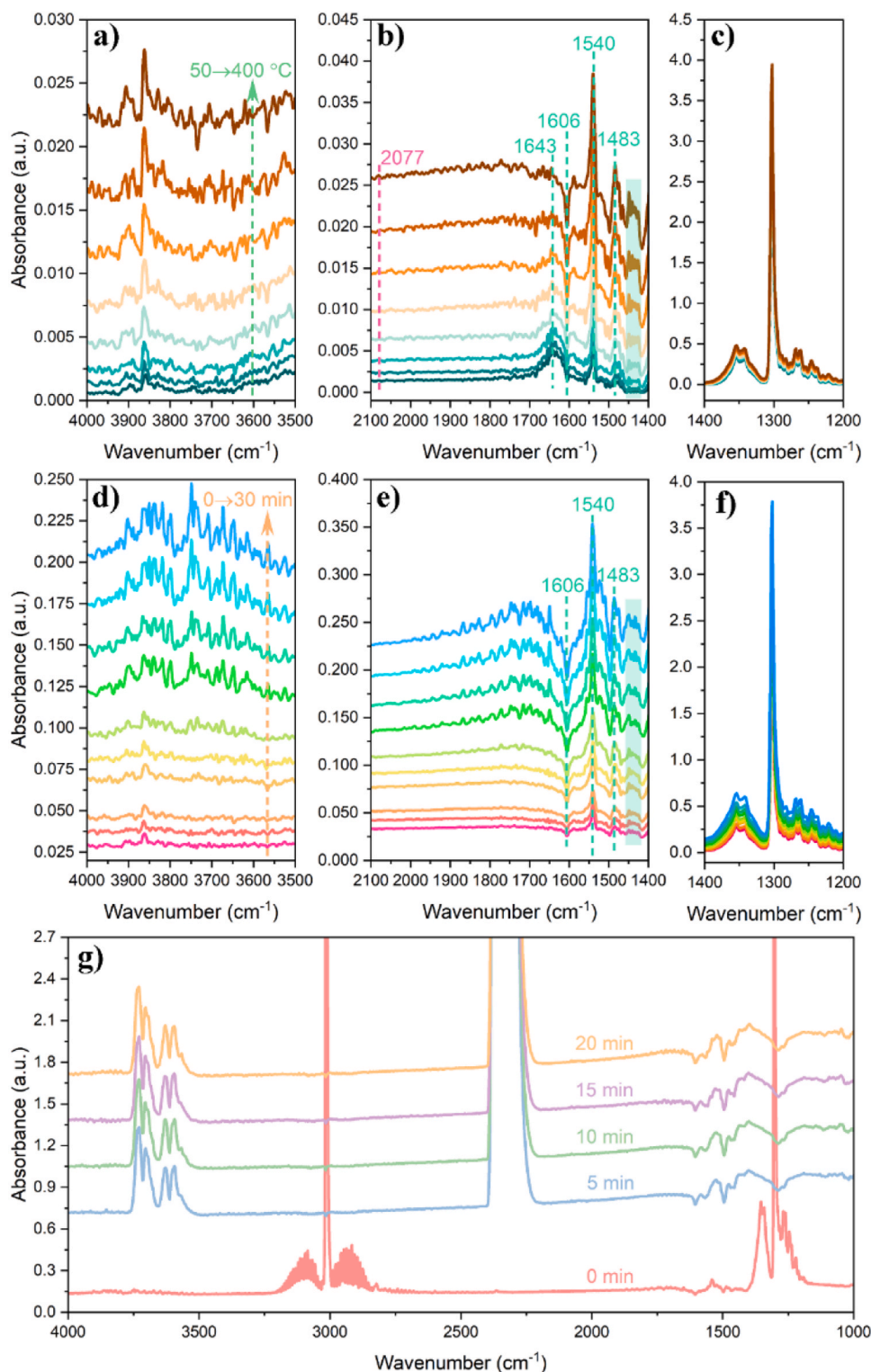
Fig. 10. *in situ* DRIFT spectra of CH_4/CO_2 temperature-programmed reaction experiment over NZ-R0 (a1-a5) and NZ-R240 (b1-b5) at the range of 50–400 °C; *in situ* DRIFT spectra of the DRM reaction over NZ-R0 (c1-c5) and NZ-R240 (d1-d5) at 400 °C for 30 min.

catalyst in DRM, and the related work is going on in our group.

4. Conclusions

In summary, the metastable Ni/ZrO_2 catalysts are constructed via reflux, and the effects of reflux on the structure and performance of Ni/ZrO_2 catalysts after avoiding the disturb of the residual ions introduced the high reflux pH value are explored. The catalyst without reflux consists of the mixed m and $t-ZrO_2$. With increasing the reflux time, the proportion of $t-ZrO_2$ gradually increases while the particle size of ZrO_2 decreases. When the reflux time is extended to 72 h, only the metastable $t-ZrO_2$ is present. Continuing to extend the reflux time to 240 h,

although ZrO_2 still retains the tetragonal phase, the support particle size further decreases and the pore structure is enriched. Meanwhile, the acid-base and defect sites, including Zr^{3+} and oxygen vacancies, on the catalyst surface are also enhanced after reflux. Additionally, Ni dispersion is remarkably improved with the extension of the reflux time due to the abundant pore structure and enhanced metal-support interaction. These results clearly illustrate the evaluation that prolonging the reflux time could significantly proliferate the performance of Ni/ZrO_2 catalyst. Besides, reflux could somewhat improve the anti-carbon ability but the widened gap between CH_4 dissociation and CO_2 activation would cause more carbon deposited on the catalyst. If the reaction temperature is raised to 750 °C, the catalyst with reflux for 240 h shows the robust
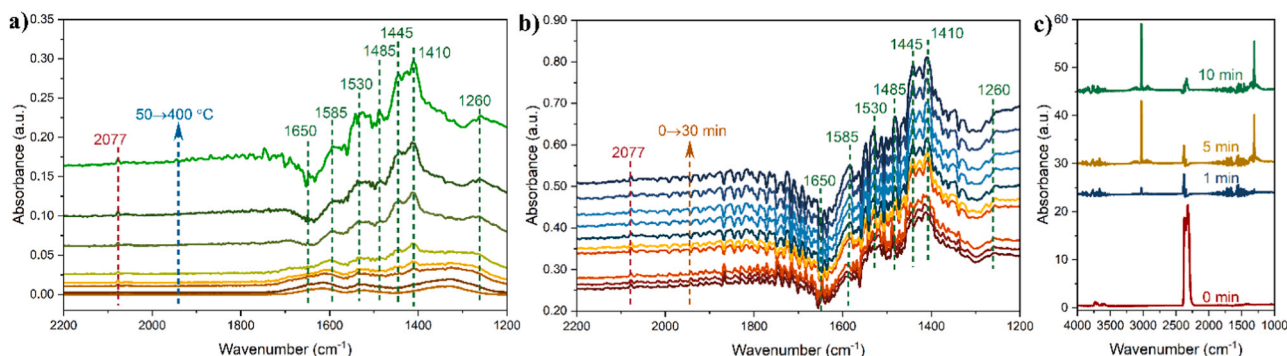
Fig. 11. (a-c) *in situ* DRIFT spectra of CH$_4$ temperature-programmed activation experiment over NZ-R240 at the range of 50–400 °C; (d-f) *in situ* DRIFT spectra of CH$_4$ activation experiment over NZ-R240 at 400 °C for 30 min; (g) *in situ* DRIFT spectra of CO$_2$ switching after CH$_4$ activation experiment.

stability for 9000 min (CH$_4$ conversion: 80 %; CO$_2$ conversion: 88 %). Moreover, the relatively low activation energies are even comparable to the noble metal catalysts, indicating the potential of the present catalyst for widespread application and intensive research. Furthermore, the bi-functional mechanisms are well demonstrated. This study would further clarify the role of metastable ZrO$_2$ in efficient and robust DRM catalyst, which could provide some references for the design of the high-

efficiency bi-functional catalyst.

CRediT authorship contribution statement

Kai Jiang: Investigation. **Tao Yang:** Writing – review & editing, Investigation, Formal analysis. **Meng Zhang:** Writing – original draft, Investigation, Formal analysis, Data curation. **Yizhuo Han:** Writing –

Fig. 12. (a) *in situ* DRIFT spectra of CO_2 temperature-programmed activation experiment over NZ-R240 at the range of 50–400 °C; (b) *in situ* DRIFT spectra of CO_2 activation experiment over NZ-R240 at 400 °C for 30 min; (c) *in situ* DRIFT spectra of CH_4 switching after CO_2 activation experiment.

review & editing, Supervision, Resources, Conceptualization. **Zhongyi Liu:** Resources, Project administration, Funding acquisition. **Jingyi Yang:** Writing – review & editing, Investigation. **Yongzhen Gao:** Investigation, Formal analysis.

Declaration of Competing Interest

The authors declare that they have no known competing financial interests or personal relationships that could have appeared to influence the work reported in this paper.

Data availability

Data will be made available on request.

Appendix A. Supporting information

Supplementary data associated with this article can be found in the online version at doi:10.1016/j.apcatb.2024.124102.

References

[1] Z. Zhang, Y. Zhang, L. Liu, Role and mechanism of calcium-based catalysts for methane dry reforming: a review, Fuel 355 (2024) 129329, https://doi.org/10.1016/j.fuel.2023.129329.

[2] I.V. Yentekakis, P. Panagiotopoulou, G. Artemakis, A review of recent efforts to promote dry reforming of methane (DRM) to syngas production via bimetallic catalyst formulations, Appl. Catal. B Environ. 296 (2021) 120210, https://doi.org/10.1016/j.apcatb.2021.120210.

[3] A. Tavasoli, G. Ozin, Green syngas by solar dry reforming, Joule 2 (2018) 571–575, https://doi.org/10.1016/j.joule.2018.02.017.

[4] X. Gao, J. Li, M. Zheng, S. Cai, J. Zhang, S. Askari, N. Dewangan, J. Ashok, S. Kawi, Recent progress in anti-coking Ni catalysts for thermo-catalytic conversion of greenhouse gases, Process Saf. Environ. Prot. 156 (2021) 598–616, https://doi.org/10.1016/j.psep.2021.10.051.

[5] G.A. Olah, A. Goeppert, M. Czaun, T. Mathew, R.B. May, G.K.S. Prakash, Single step bi-reforming and oxidative bi-reforming of methane (natural gas) with steam and carbon dioxide to metgas (CO-2H$_2$) for methanol synthesis: self-sufficient effective and exclusive oxygenation of methane to methanol with oxygen, J. Am. Chem. Soc. 137 (2015) 8720–8729, https://doi.org/10.1021/jacs.5b02029.

[6] M. Usman, W. Daud, H.F. Abbas, Dry reforming of methane: influence of process parameters-A review, Renew. Sustain. Energy Rev. 45 (2015) 710–744, https://doi.org/10.1016/j.rser.2015.02.026.

[7] A. Abdulrasheed, A.A. Jalil, Y. Gambo, M. Ibrahim, H.U. Hambali, M.Y.S. Hamill, A review on catalyst development for dry reforming of methane to syngas: recent advances, Renew. Sustain. Energy Rev. 108 (2019) 175–193, https://doi.org/10.1016/j.rser.2019.03.054.

[8] D. Pakhare, J. Spivey, A review of dry (CO$_2$) reforming of methane over noble metal catalysts, Chem. Soc. Rev. 43 (2014) 7813–7837, https://doi.org/10.1039/c3cs60395d.

[9] S.E. Golunski, Why use platinum in catalytic converters?, 162-162, Platin. Met. Rev. 51 (2007), https://doi.org/10.1595/147106707×205857.

[10] O. Muraza, A. Galadima, A review on coke management during dry reforming of methane, Int. J. Energy Res. 39 (2015) 1196–1216, https://doi.org/10.1002/er.3295.

[11] X. Gao, J. Ashok, S. Kawi, A review on roles of pretreatment atmospheres for the preparation of efficient Ni-based catalysts, Catal. Today 397-399 (2022) 581–591, https://doi.org/10.1016/j.cattod.2021.06.009.

[12] M. Zhang, J. Zhang, Z. Zhou, S. Chen, T. Zhang, F. Song, Q. Zhang, N. Tsubaki, Y. Tan, Y. Han, Effects of the surface adsorbed oxygen species tuned by rare-earth metal doping on dry reforming of methane over Ni/ZrO$_2$ catalyst, Appl. Catal. B Environ. 264 (2020) 118522, https://doi.org/10.1016/j.apcatb.2019.118522.

[13] S. Kuboon, J. Deng, M. Gao, K. Faungnawakij, J.-y Hasegawa, X. Zhang, L. Shi, D. Zhang, Unraveling the promotional effects of NiCo catalysts over defective boron nitride nanosheets in dry reforming of methane, Catal. Today 402 (2022) 283–291, https://doi.org/10.1016/j.cattod.2022.04.031.

[14] J. Yu, T. Le, D. Jing, E. Stavitski, N. Hunter, K. Lalit, D. Leshchev, D.E. Resasco, E. H. Sargent, B. Wang, W. Huang, Balancing elementary steps enables coke-free dry reforming of methane, Nat. Commun. 14 (2023) 7514, https://doi.org/10.1038/s41467-023-43277-0.

[15] M. Zhang, X. Zhou, J. Yang, T. Yang, Z. Liu, Y. Han, Deciphering the ZrO$_2$ phase engineering effects on dry reforming of methane over the Ni/ZrO$_2$ catalysts, Fuel 349 (2023) 128705, https://doi.org/10.1016/j.fuel.2023.128705.

[16] Y. Fu, Y. Sun, CH$_4$-CO$_2$ reforming: challenges and outlook, Sci. Sin. Chim. 50 (2020) 816–831, https://doi.org/10.1360/SSC-2019-0160.

[17] S. Liu, C. Dun, M. Shah, J. Chen, S. Rao, J. Wei, E.A. Kyriakidou, J.J. Urban, M. T. Swihart, Producing ultrastable Ni-ZrO$_2$ nanoshell catalysts for dry reforming of methane by flame synthesis and Ni exsolution, Chem. Catal. 2 (2022) 2262–2274, https://doi.org/10.1016/j.checat.2022.05.013.

[18] W.Z. Li, Z.K. Zhao, G.R. Wang, Modulating morphology and textural properties of ZrO$_2$ for supported Ni catalysts toward dry reforming of methane, AIChE J. 63 (2017) 2900–2915, https://doi.org/10.1002/aic.15661.

[19] M. Zhang, J.F. Zhang, X.P. Zhang, Z.L. Zhou, F. Song, Q.D. Zhang, Y.S. Tan, Y. Z. Han, How the reflux treatment stabilizes the metastable structure of ZrO$_2$ and improves the performance of Ni/ZrO$_2$ catalyst for dry reforming of methane? Energy Convers. Manag. 216 (2020) 112950 https://doi.org/10.1016/j.enconman.2020.112950.

[20] T. Xiao, X. Liu, G. Xu, Y. Zhang, Phase tuning of ZrO$_2$ supported cobalt catalysts for hydrodeoxygenation of 5-hydroxymethylfurfural to 2,5-dimethylfuran under mild conditions, Appl. Catal. B Environ. 295 (2021) 120270, https://doi.org/10.1016/j.apcatb.2021.120270.

[21] Y. Zhou, L. Liu, G. Li, C. Hu, Insights into the influence of ZrO$_2$ crystal structures on methyl laurate hydrogenation over Co/ZrO$_2$ catalysts, ACS Catal. 11 (2021) 7099–7113, https://doi.org/10.1021/acscatal.1c00632.

[22] E. Hong, C. Kim, D.H. Lim, H.J. Cho, C.H. Shin, Catalytic methane combustion over Pd/ZrO$_2$ catalysts: effects of crystalline structure and textural properties, Appl. Catal. B Environ. 232 (2018) 544–552, https://doi.org/10.1016/j.apcatb.2018.03.101.

[23] N. Sun, X. Wen, F. Wang, W. Wei, Y. Sun, Effect of pore structure on Ni catalyst for CO$_2$ reforming of CH$_4$, Energy Environ. Sci. 3 (2010) 366–369, https://doi.org/10.1039/B925503F.

[24] M. Rezaei, S.M. Alavi, S. Sahebdelfar, P. Bai, X.M. Liu, Z.F. Yan, CO$_2$ reforming of CH$_4$ over nanocrystalline zirconia-supported nickel catalysts, Appl. Catal. B Environ. 77 (2008) 346–354, https://doi.org/10.1016/j.apcatb.2007.08.004.

[25] W.Z. Li, H. Huang, H.J. Li, W. Zhang, H.C. Liu, Facile synthesis of pure monoclinic and tetragonal zirconia nanoparticles and their phase effects on the behavior of supported molybdena catalysts for methanol-selective oxidation, Langmuir 24 (2008) 8358–8366, https://doi.org/10.1021/la800370r.

[26] S. Wang, K.H. Yin, Y.C. Zhang, H.C. Liu, Glycerol hydrogenolysis to propylene glycol and ethylene glycol on zirconia supported noble metal catalysts, ACS Catal. 3 (2013) 2112–2121, https://doi.org/10.1021/cs400486z.

[27] Q. Yuan, L.-L. Li, S.-L. Lu, H.-H. Duan, Z.-X. Li, Y.-X. Zhu, C.-H. Yan, Facile synthesis of Zr-based functional materials with highly ordered mesoporous structures, J. Phys. Chem. C 113 (2009) 4117–4124, https://doi.org/10.1021/jp806467c.

[28] X. Zhou, Y. Gao, J. Yang, W. Yi, Q. Pang, Z. Liu, B. Liu, M. Zhang, Unraveling the effects of Ce/Zr molar ratio in mesoporous Ce$_x$Zr$_{1-x}$O$_2$ on the performance of dry reforming of methane over the supported Ni catalysts, Chem. Eng. Res. Des. 193 (2023) 626–640, https://doi.org/10.1016/j.cherd.2023.04.020.

[29] J. Shao, C. Li, Z. Fei, Y. Liu, J. Zhang, L. Li, MOFs-derived Ni@ZrO$_2$ catalyst for dry reforming of methane: tunable metal-support interaction, Mol. Catal. 558 (2024) 114028, https://doi.org/10.1016/j.mcat.2024.114028.

[30] J. Liu, Y. He, L. Yan, K. Li, C. Zhang, H. Xiang, X. Wen, Y. Li, Nano-sized ZrO_2 derived from metal-organic frameworks and their catalytic performance for aromatic synthesis from syngas, Catal. Sci. Technol. 9 (2019) 2982–2992, https://doi.org/10.1039/C9CY00453J.

[31] S.F. Yin, B.Q. Xu, On the preparation of high-surface-area nano-zirconia by reflux-digestion of hydrous zirconia gel in basic solution, ChemPhysChem 4 (2003) 277–281, https://doi.org/10.1002/cphc.200390044.

[32] G.K. Chuah, S. Jaenicke, S.A. Cheong, K.S. Chan, The influence of preparation conditions on the surface area of zirconia, Appl. Catal. A Gen. 145 (1996) 267–284, https://doi.org/10.1016/0926-860x(96)00152-4.

[33] K.T. Jung, A.T. Bell, The effects of synthesis and pretreatment conditions on the bulk structure and surface properties of zirconia, J. Mol. Catal. A Chem. 163 (2000) 27–42, https://doi.org/10.1016/s1381-1169(00)00397-6.

[34] Y. Wang, Q. Zhao, Y. Wang, C. Hu, P. Da Costa, One-step synthesis of highly active and stable Ni-ZrO_x for dry reforming of methane, Ind. Eng. Chem. Res. 59 (2020) 11441–11452, https://doi.org/10.1021/acs.iecr.0c01416.

[35] S.-F. Yin, B.-Q. Xu, S.-J. Wang, C.-T. Au, Nanosized Ru on high-surface-area superbasic ZrO_2-KOH for efficient generation of hydrogen via ammonia decomposition, Appl. Catal. A Gen. 301 (2006) 202–210, https://doi.org/10.1016/j.apcata.2005.12.005.

[36] G.K. Chuah, An investigation into the preparation of high surface area zirconia, Catal. Today 49 (1999) 131–139, https://doi.org/10.1016/S0920-5861(98)00417-9.

[37] Y. Wang, W.Z. Gao, S. Kazumi, H.J. Li, G.H. Yang, N. Tsubaki, Direct and oriented conversion of CO_2 into value-added aromatics, Chem.-Eur. J 25 (2019) 5149–5153, https://doi.org/10.1002/chem.201806165.

[38] B. Safavinia, Y. Wang, C. Jiang, C. Roman, P. Darapaneni, J. Larriviere, D. A. Cullen, K.M. Dooley, J.A. Dorman, Enhancing $Ce_xZr_{1-x}O_2$ activity for methane dry reforming using subsurface Ni dopants, ACS Catal. 10 (2020) 4070–4079, https://doi.org/10.1021/acscatal.0c00203.

[39] M.S. Ferrandon, C. Byron, G. Celik, Y. Zhang, C. Ni, J. Sloppy, R.A. McCormick, K. Booksh, A.V. Teplyakov, M. Delferro, Grafted nickel-promoter catalysts for dry reforming of methane identified through high-throughput experimentation, Appl. Catal. A Gen. 629 (2022) 118379, https://doi.org/10.1016/j.apcata.2021.118379.

[40] T. Zhang, Z. Liu, Y.-A. Zhu, Z. Liu, Z. Sui, K. Zhu, X. Zhou, Dry reforming of methane on Ni-Fe-MgO catalysts: Influence of Fe on carbon-resistant property and kinetics, Appl. Catal. B Environ. 264 (2020) 118497, https://doi.org/10.1016/j.apcatb.2019.118497.

[41] Y. Wang, L. Li, G. Li, Q. Zhao, Xs Wu, Y. Wang, Y. Sun, C. Hu, Synergy of oxygen vacancies and Ni^0 species to promote the stability of a Ni/ZrO_2 catalyst for dry reforming of methane at low temperatures, ACS Catal. 13 (2023) 6486–6496, https://doi.org/10.1021/acscatal.2c06412.

[42] M. Zhang, J. Zhang, Z. Zhou, Q. Zhang, Y. Tan, Y. Han, Effects of calcination atmosphere on the performance of the co-precipitated Ni/ZrO_2 catalyst in dry reforming of methane, Can. J. Chem. Eng. 100 (2021) 172–183, https://doi.org/10.1002/cjce.24129.

[43] M. Zhang, J.F. Zhang, Y.Q. Wu, J.X. Pan, Q.D. Zhang, Y.S. Tan, Y.Z. Han, Insight into the effects of the oxygen species over Ni/ZrO_2 catalyst surface on methane reforming with carbon dioxide, Appl. Catal. B Environ. 244 (2019) 427–437, https://doi.org/10.1016/j.apcatb.2018.11.068.

[44] D. He, S. Wu, X. Cao, D. Chen, L. Zhang, Y. Zhang, Y. Luo, Dynamic trap of Ni at elevated temperature for yielding high-efficiency methane dry reforming catalyst, Appl. Catal. B Environ. 346 (2024) 123728, https://doi.org/10.1016/j.apcatb.2024.123728.

[45] X.P. Zhang, Q.D. Zhang, N. Tsubaki, Y.S. Tan, Y.Z. Han, Carbon dioxide reforming of methane over Ni nanoparticles incorporated into mesoporous amorphous ZrO_2 matrix, Fuel 147 (2015) 243–252, https://doi.org/10.1016/j.fuel.2015.01.076.

[46] R. Zhou, M. Mohamedali, Y. Ren, Q. Lu, N. Mahinpey, Facile synthesis of multi-layered nanostructured Ni/CeO_2 catalyst plus in-situ pre-treatment for efficient dry reforming of methane, Appl. Catal. B Environ. 316 (2022) 121696, https://doi.org/10.1016/j.apcatb.2022.121696.

[47] J. Deng, K. Bu, Y. Shen, X. Zhang, J. Zhang, K. Faungnawakij, D. Zhang, Cooperatively enhanced coking resistance via boron nitride coating over Ni-based catalysts for dry reforming of methane, Appl. Catal. B Environ. 302 (2021) 120859, https://doi.org/10.1016/j.apcatb.2021.120859.

[48] P.M. de Souza, R.C. Rabelo-Neto, L.E.P. Borges, G. Jacobs, B.H. Davis, U. M. Graham, D.E. Resasco, F.B. Noronha, Effect of zirconia morphology on hydrodeoxygenation of phenol over Pd/ZrO_2, ACS Catal. 5 (2015) 7385–7398, https://doi.org/10.1021/acscatal.5b01501.

[49] H. Muroyama, Y. Tsuda, T. Asakoshi, H. Masitah, T. Okanishi, T. Matsui, K. Eguchi, Carbon dioxide methanation over Ni catalysts supported on various metal oxides, J. Catal. 343 (2016) 178–184, https://doi.org/10.1016/j.jcat.2016.07.018.

[50] X. Yao, Q. Cheng, Y. Attada, S. Ould-Chikh, A. Ramírez, X. Bai, H.O. Mohamed, G. Li, G. Shterk, L. Zheng, J. Gascon, Y. Han, O.M. Bakr, P. Castaño, Atypical stability of exsolved Ni-Fe alloy nanoparticles on double layered perovskite for CO_2 dry reforming of methane, Appl. Catal. B Environ. 328 (2023) 122479, https://doi.org/10.1016/j.apcatb.2023.122479.

[51] F. Zhang, Z. Liu, X. Chen, N. Rui, L.E. Betancourt, L. Lin, W. Xu, C.-j Sun, A.M. M. Abeykoon, J.A. Rodriguez, J. Teržan, K. Lorber, P. Djinović, S.D. Senanayake, Effects of Zr doping into ceria for the dry reforming of methane over Ni/$CeZrO_2$ catalysts: in situ studies with XRD, XAFS, and AP-XPS, ACS Catal. 10 (2020) 3274–3284, https://doi.org/10.1021/acscatal.9b04451.

[52] Y.J. Zhang, Y.Y. Zhan, C.Q. Chen, Y.N. Cao, X.Y. Lin, Q. Zheng, Highly efficient Au/ZrO_2 catalysts for low-temperature water-gas shift reaction: effect of pre-calcination temperature of ZrO_2, Int. J. Hydrog. Energy 37 (2012) 12292–12300, https://doi.org/10.1016/j.ijhydene.2012.06.025.

[53] X. Li, Z. Yang, L. Zhang, Z. He, Y. Yan, J. Ran, Z.C. Kadirova, Influence of ZrO_2 crystal structure on the catalytic performance of Fe-Ni catalysts for CO_2-assisted ethane dehydrogenation reaction, Fuel 322 (2022) 124122, https://doi.org/10.1016/j.fuel.2022.124122.

[54] C. Huang, C. Zhu, M. Zhang, Y. Lu, Q. Wang, H. Qian, J. Chen, K. Fang, Direct conversion of syngas to higher alcohols over a CuCoAl||t-ZrO_2 multifunctional catalyst, ChemCatChem 13 (2021) 3184–3197, https://doi.org/10.1002/cctc.202100293.

[55] A.S. Al-Fatesh, Y. Arafat, S.O. Kasim, A.A. Ibrahim, A.E. Abasaeed, A.H. Fakeeha, In situ auto-gasification of coke deposits over a novel Ni-Ce/W-Zr catalyst by sequential generation of oxygen vacancies for remarkably stable syngas production via CO_2-reforming of methane, Appl. Catal. B Environ. 280 (2021) 119445, https://doi.org/10.1016/j.apcatb.2020.119445.

[56] C. Jiang, E. Loisel, D.A. Cullen, J.A. Dorman, K.M. Dooley, On the enhanced sulfur and coking tolerance of Ni-Co-rare earth oxide catalysts for the dry reforming of methane, J. Catal. 393 (2021) 215–229, https://doi.org/10.1016/j.jcat.2020.11.028.

[57] Y. Pan, X. Xu, Y. Zhong, L. Ge, Y. Chen, J.-P.M. Veder, D. Guan, R. O'Hayre, M. Li, G. Wang, H. Wang, W. Zhou, Z. Shao, Direct evidence of boosted oxygen evolution over perovskite by enhanced lattice oxygen participation, Nat. Commun. 11 (2020) 2002, https://doi.org/10.1038/s41467-020-15873-x.

[58] G. Li, Z. Shui, X. Duan, H. Yang, Z. Zhao, T. Zhao, Z. Zhang, G. Jiang, H. Ren, J. Cheng, Z. Hao, Unveiling the balance between catalytic activity and water resistance over Co_3O_4 catalysts for propane oxidation: the role of crystal facet and oxygen vacancy, ACS Catal. 13 (2023) 237–247, https://doi.org/10.1021/acscatal.2c05640.

[59] J.W. Xu, Y. Zhang, X.L. Xu, X.Z. Fang, R. Xi, Y.M. Liu, R.Y. Zheng, X. Wang, Constructing $La_2B_2O_7$ (B = Ti, Zr, Ce) compounds with three typical crystalline phases for the oxidative coupling of methane: the effect of phase structures, superoxide anions, and alkalinity on the reactivity, ACS Catal. 9 (2019) 4030–4045, https://doi.org/10.1021/acscatal.9b00022.

[60] G.K. Chuah, S. Jaenicke, B.K. Pong, The preparation of high-surface-area zirconia II. Influence of precipitating agent and digestion on the morphology and microstructure of hydrous zirconia, J. Catal. 175 (1998) 80–92, https://doi.org/10.1006/jcat.1998.1980.

[61] F.G. Wang, K.H. Han, L.L. Xu, H. Yu, W.D. Shi, Ni/SiO_2 catalyst prepared by strong electrostatic adsorption for a low-temperature methane dry reforming reaction, Ind. Eng. Chem. Res. 60 (2021) 3324–3333, https://doi.org/10.1021/acs.iecr.0c06020.

[62] V.R. Choudhary, K.C. Mondal, A.S. Mamman, U.A. Joshi, Carbon-free dry reforming of methane to syngas over $NdCoO_3$ perovskite-type mixed metal oxide catalyst, Catal. Lett. 100 (2005) 271–276, https://doi.org/10.1007/s10562-004-3467-0.

[63] Q. Ma, Y. Han, Q. Wei, S. Makpal, X. Gao, J. Zhang, T.-s Zhao, Stabilizing Ni on bimodal mesoporous-macroporous alumina with enhanced coke tolerance in dry reforming of methane to syngas, J. CO2 Util. 35 (2020) 288–297, https://doi.org/10.1016/j.jcou.2019.10.010.

[64] S.X. Lin, J. Wang, Y.Y. Mi, S.Y. Yang, Z. Wang, W.M. Liu, D.S. Wu, H.G. Peng, Trifunctional strategy for the design and synthesis of a Ni-CeO_2@SiO_2 catalyst with remarkable low-temperature sintering and coking resistance for methane dry reforming, Chin. J. Catal. 42 (2021) 1808–1820, https://doi.org/10.1016/s1872-2067(21)63789-0.

[65] M.K. Nikoo, N.A.S. Amin, Thermodynamic analysis of carbon dioxide reforming of methane in view of solid carbon formation, Fuel Process. Technol. 92 (2011) 678–691, https://doi.org/10.1016/j.fuproc.2010.11.027.

[66] D. Pakhare, V. Schwartz, V. Abdelsayed, D. Haynes, D. Shekhawat, J. Poston, J. Spivey, Kinetic and mechanistic study of dry (CO_2) reforming of methane over Rh-substituted $La_2Zr_2O_7$ pyrochlores, J. Catal. 316 (2014) 78–92, https://doi.org/10.1016/j.jcat.2014.04.023.

[67] X. Zhang, J. Deng, T. Lan, Y. Shen, Q. Zhong, W. Ren, D. Zhang, Promoting methane dry reforming over Ni catalysts via modulating surface electronic structures of BN supports by doping carbon, ACS Catal. 12 (2022) 14152–14161, https://doi.org/10.1021/acscatal.2c04800.

[68] L. Ma, R. Ye, Y. Huang, T.R. Reina, X. Wang, C. Li, X.L. Zhang, M. Fan, R. Zhang, J. Liu, Enhanced low-temperature CO_2 methanation performance of Ni/ZrO_2 catalysts via a phase engineering strategy, Chem. Eng. J. 446 (2022) 137031, https://doi.org/10.1016/j.cej.2022.137031.

[69] K.K. Bu, S. Kuboon, J. Deng, H.R. Li, T.T. Yan, G.R. Chen, L.Y. Shi, D.S. Zhang, Methane dry reforming over boron nitride interface-confined and LDHs-derived Ni catalysts, Appl. Catal. B Environ. 252 (2019) 86–97, https://doi.org/10.1016/j.apcatb.2019.04.007.

[70] Y. Wang, L. Yao, Y.N. Wang, S.H. Wang, Q. Zhao, D.H. Mao, C.W. Hu, Low-temperature catalytic CO_2 dry reforming of methane on Ni-Si/ZrO_2 catalyst, ACS Catal. 8 (2018) 6495–6506, https://doi.org/10.1021/acscatal.8b00584.

[71] H. Takano, Y. Kirihata, K. Izumiya, N. Kumagai, H. Habazaki, K. Hashimoto, Highly active Ni/Y-doped ZrO_2 catalysts for CO_2 methanation, Appl. Surf. Sci. 388 (2016) 653–663, https://doi.org/10.1016/j.apsusc.2015.11.187.

[72] L. Azancot, L.F. Bobadilla, M.A. Centeno, J.A. Odriozola, IR spectroscopic insights into the coking-resistance effect of potassium on nickel-based catalyst during dry reforming of methane, Appl. Catal. B Environ. 285 (2021) 119822, https://doi.org/10.1016/j.apcatb.2020.119822.

[73] Y. Tang, Y.C. Wei, Z.Y. Wang, S.R. Zhang, Y.T. Li, L. Nguyen, Y.X. Li, Y. Zhou, W. J. Shen, F.F. Tao, P.J. Hu, Synergy of single-atom Ni_1 and Ru_1 sites on CeO_2 for dry reforming of CH_4, J. Am. Chem. Soc. 141 (2019) 7283–7293, https://doi.org/10.1021/jacs.8b10910.

[74] C. He, Y. Gong, S. Li, J. Wu, Z. Lu, Q. Li, L. Wang, S. Wu, J. Zhang, Single-atom alloys materials for CO_2 and CH_4 catalytic conversion, Adv. Mater. n/a (2024) 2311628, https://doi.org/10.1002/adma.202311628.

[75] M. Zhang, X. Zhou, C. Li, W. Yi, Q. Gao, J. Zhang, Q. Zhang, Y. Han, Ni/Y_2O_3-ZrO_2 catalysts for dry reforming of methane: increased Y content boosted the performance via enhancing metal-support interaction and surface oxygen species, Fuel 340 (2023) 127543, https://doi.org/10.1016/j.fuel.2023.127543.

[76] Y. Zhang, Y. Zu, D. He, J. Liang, L. Zhu, Y. Mei, Y. Luo, The tailored role of "defect" sites on γ-alumina: a key to yield an efficient methane dry reforming catalyst with

superior nickel utilization, Appl. Catal. B Environ. 315 (2022) 121539, https://doi.org/10.1016/j.apcatb.2022.121539.

[77] Y.X. Bai, J.F. Zhang, G.H. Yang, Q.D. Zhang, J.X. Pan, H.J. Xie, X.C. Liu, Y.Z. Han, Y.S. Tan, Insight into the nanoparticle growth in supported Ni catalysts during the early stage of CO hydrogenation reaction: the important role of adsorbed CO molecules, ACS Catal. 8 (2018) 6367–6374, https://doi.org/10.1021/acscatal.8b00835.